
Electrical Engineering Theses

Electrical Engineering

Spring 3-23-2015

Stochastic Assessment of Bone Fragility in Human Lumbar Spine

Rajeshwar Rao Pinninti

Follow this and additional works at: https://scholarworks.uttyler.edu/ee_grad



Part of the [Electrical and Computer Engineering Commons](#)

Recommended Citation

Pinninti, Rajeshwar Rao, "Stochastic Assessment of Bone Fragility in Human Lumbar Spine" (2015).

Electrical Engineering Theses. Paper 26.

<http://hdl.handle.net/10950/256>

This Thesis is brought to you for free and open access by the Electrical Engineering at Scholar Works at UT Tyler. It has been accepted for inclusion in Electrical Engineering Theses by an authorized administrator of Scholar Works at UT Tyler. For more information, please contact tgullings@uttyler.edu.

STOCHASTIC ASSESSMENT OF BONE FRAGILITY IN HUMAN LUMBAR SPINE

by

RAJESHWAR RAO PINNINTI

A thesis submitted in partial fulfillment
of the requirements for the degree of
Masters of Science in Electrical Engineering
Department of Electrical Engineering

Mukul Shirvaikar, Ph.D., Committee Chair

College of Engineering and Computer Science

The University of Texas at Tyler
May 2015

The University of Texas at Tyler
Tyler, Texas

This is to certify that the Master's thesis of

RAJESHWAR RAO PINNINTI

has been approved for the thesis requirements on
December 4th, 2014
for the Master of Science in Electrical Engineering

Approvals:



Thesis Chair: Dr. Mukul V. Shirvaikar, Ph.D.



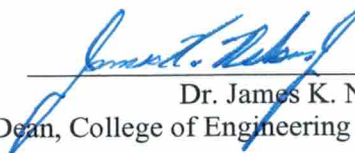
Member: Dr. X. Neil Dong, Ph.D.



Member: Dr. Ron J. Pieper, Ph.D.



Chair and Graduate Coordinator: Dr. Hassan El-Kishky, Ph.D.



Dr. James K. Nelson, Jr., Ph.D., P.E.,
Dean, College of Engineering and Computer Science

ACKNOWLEDGEMENTS

I would like to express my gratitude to my parents and family members for their constant encouragement and financial support to pursue my master of science in Electrical Engineering. I would like to express my gratitude to Dr. Mukul Shirvaikar and Dr. Xuanliang Dong for giving me this wonderful opportunity to work on medical image processing. I am grateful to them for their exceptional guidance, encouragement, support and patience to complete my thesis successfully. I would also like to express my gratitude to Dr. Ron Pieper for taking time to be a part of my committee member and for reviewing my thesis document.

This study was financially supported by the NIH/NIAMS under award number R15AR061740. In addition, this work received computation support from Computational System Biology Core at the University of Texas at San Antonio, funded by the NIH/NIMHD under award number G12MD007591.

I would like to thank each and every person for their encouragement and support to complete my thesis work successfully.

TABLE OF CONTENTS

List of Tables	iv
List of Figures	v
Abstract	vii
Chapter One - Introduction	1
1.1 Imaging modalities available in clinical applications and basic science research	1
1.2 Various imaging techniques to enhance the prediction of bone fractures from 2D-projection images	2
1.3 Objective and framework	3
1.4 Organization of thesis	4
Chapter Two - Past Work	5
Chapter Three - Technical Background	12
3.1 Dual-Energy X-ray absorptiometry (DXA)	12
3.2 Micro-computed tomography (Micro-CT)	13
3.3 Experimental variogram	14
3.3.1 Correlation length or range (L)	15
3.3.2 Sill variance (C)	16
3.3.3 Nugget variance (C_0)	16
3.4 Microarchitecture parameters of trabecular bone	16
3.4.1 Bone volume fraction (BV/TV)	16
3.4.2 Trabecular thickness (Tb.Th)	17
3.4.3 Trabecular separation (Tb.Sp)	17

3.4.4 Trabecular number (Tb.N)	17
3.4.5 Connectivity density (Conn.Dn)	17
3.4.6 Bone surface to volume ratio (BS/BV)	18
3.4.7 Structure model index (SMI)	18
3.4.8 Trabecular bone pattern factor (Tb. P_f)	18
3.4.9 Degree of anisotropy (DA)	18
Chapter Four - Methods and Experimental Procedures	20
4.1 DXA image acquisition.....	20
4.2 BMD map extraction from DXA scans	22
4.3 Stochastic assessment of BMD map	23
4.4 Micro-CT image acquisition	25
4.5 Measuring microarchitecture parameters of trabecular bone.....	26
4.6 Statistical analysis	28
4.6.1 Linear regression analysis	28
4.6.2 Correlation test.....	29
Chapter Five - Results.....	30
5.1 Microarchitecture parameters calculated from micro-CT images	30
5.2 DXA and stochastic parameters of vertebrae.....	31
5.3 Pearson correlation coefficient analysis of stochastic, microarchitecture and DXA parameters	32
5.4 Linear regression analysis of DXA, stochastic and microarchitecture parameters	33
Chapter Six - Discussion and Conclusion.....	49
6.1 DXA measurements of human lumbar vertebrae.....	49
6.2 Microarchitecture parameters within the vertebral body	50

6.3 Correlations between stochastic predictors and microarchitecture parameters	50
6.4 Comparison of stochastic assessment with existing imaging techniques	51
6.5 Limitations and future work.....	53
6.6 Conclusion	54
References	55
Appendix A - Calculation of P-values for correlation analysis	61
Appendix B - MATLAB code	63

LIST OF TABLES

Table 2.1 Summary of selected previous studies	11
Table 3.1 Stochastic parameters of experimental variogram.....	16
Table 3.2 Microarchitecture parameters of trabecular bone	19
Table 5.1 Microarchitecture parameters of lumbar vertebral bodies	30
Table 5.2 DXA and stochastic parameters of vertebrae	31
Table 5.3 Descriptive statistics of DXA and stochastic parameters	31
Table 5.4 Descriptive statistics of microarchitecture parameters	32
Table 5.5 Pearson correlation coefficients between stochastic and microarchitecure parameters	32
Table 5.6 Pearson correlation coefficients between DXA, stochastic and microarchitecture parameters.....	33

LIST OF FIGURES

Figure 3.1 Dual energy X-ray absorptiometry machine	13
Figure 3.2 Micro computed tomography machine.....	14
Figure 3.3 Theoretical exponential model (left) and hole-effect model (right) fitted over the experimental variogram of the bone mineral density map.....	15
Figure 4.1 Gray scale image of DXA scan of lumbar vertebra (L3) in PA-direction.....	21
Figure 4.2 Sequence of steps to obtain the stochastic parameters of vertebrae DXA scans	22
Figure 4.3 BMD map of lumbar vertebra (L3) in PA-direction	23
Figure 4.4 Color map of vertebra BMD map in PA-direction (left), hole-effect model is fitted over experimental variogram of BMD map (right)	24
Figure 4.5 Gray scale images of a vertebral body obtained from μ CT (a) Coronal cross-section (left side) (b) Axial cross-section (right side).....	25
Figure 4.6 Binary images of a vertebra (a) Coronal cross-section (left side) (b) Axial cross-section (right side)	26
Figure 4.7 Sequence of steps to evaluate microarchitecture parameters of specimens	27
Figure 5.1 Linear regression analysis of sill variance and bone volume fraction.....	34
Figure 5.2 Linear regression analysis of sill variance and bone surface to volume ratio	34
Figure 5.3 Linear regression analysis of sill variance and trabecular thickness	35
Figure 5.4 Linear regression analysis of sill variance and trabecular number.....	35
Figure 5.5 Linear regression analysis of sill variance and trabecular separation	36
Figure 5.6 Linear regression analysis of sill variance and connectivity density	36
Figure 5.7 Linear regression analysis of bone volume fraction and surface to volume ratio	37
Figure 5.8 Linear regression analysis of bone volume fraction and trabecular thickness	37
Figure 5.9 Linear regression analysis of bone volume fraction and trabecular number...	38

Figure 5.10 Linear regression analysis of bone volume fraction and trabecular separation	38
Figure 5.11 Linear regression analysis of bone volume fraction and connectivity density	39
Figure 5.12 Linear regression analysis of surface to volume ratio and trabecular thickness	39
Figure 5.13 Linear regression analysis of surface to volume ratio and trabecular number	40
Figure 5.14 Linear regression analysis of bone surface to volume ratio and trabecular separation	40
Figure 5.15 Linear regression analysis of surface to volume ratio and connectivity density	41
Figure 5.16 Linear regression analysis of trabecular thickness and trabecular number ...	41
Figure 5.17 Linear regression analysis of trabecular thickness and trabecular separation	42
Figure 5.18 Linear regression analysis of trabecular thickness and connectivity density	42
Figure 5.19 Linear regression analysis of trabecular number and trabecular separation..	43
Figure 5.20 Linear regression analysis of trabecular number and connectivity density...	43
Figure 5.21 Linear regression analysis of trabecular separation and connectivity density	44
Figure 5.22 Linear regression analysis of sill variance and bone mineral density	44
Figure 5.23 Linear regression analysis of correlation length and nugget variance	45
Figure 5.24 Linear regression analysis of area of specimen and bone volume fraction...	45
Figure 5.25 Linear regression analysis of area of specimen and surface to volume ratio	46
Figure 5.26 Linear regression analysis of area of specimen and trabecular thickness	46
Figure 5.27 Linear regression analysis of area of specimen and trabecular separation....	47
Figure 5.28 Linear regression analysis of area and bone mineral content of the vertebrae	47
Figure 5.29 Linear regression analysis of bone mineral content and bone mineral density	48
Figure 5.30 Linear regression analysis of DXA-BMD and BMD calculated.....	48

ABSTRACT

STOCHASTIC ASSESSMENT OF BONE FRAGILITY IN HUMAN LUMBAR SPINE

Rajeshwar Rao Pinninti

Thesis Chair: Mukul Shirvaikar, Ph. D.

The University of Texas at Tyler
May 2015

Osteoporotic fractures are a vital public health concern and create a great economic burden for our society. It is estimated that more than 2 million fractures occur in the United States at a cost of \$17 billion each year. Deterioration of microarchitecture of trabecular bone is considered as a major contributor to bone fragility. Current clinical imaging modalities such as Dual-energy X-ray absorptiometry (DXA) are not able to describe bone microarchitecture due to their low resolution. The main objective of this study was to obtain the relationship between stochastic parameters calculated from bone mineral density (BMD) maps of DXA scans and the microarchitecture parameters measured from three dimensional (3D) images of human lumbar vertebrae acquired using a Micro-Computed Tomography (Micro-CT) scanner.

Eighteen human lumbar vertebrae with intact posterior elements were scanned in the posterior-anterior projection using a DXA scanner. Stochastic parameters such as correlation length (L), sill variance (C) and nugget variance (C_0) were calculated by fitting a theoretical model onto the experimental variogram of the BMD map of the human vertebrae. In addition, microarchitecture parameters such as bone volume fraction (BV/TV), trabecular thickness (Tb.Th), trabecular separation (Tb.Sp), trabecular number (Tb.N), connectivity density (Conn.Dn), and bone surface-to-volume ratio (BS/BV) were measured from 3D images of the same human lumbar vertebrae.

Significant correlations were observed between stochastic predictors and microarchitecture parameters of trabecular bone. Specifically, the sill variance was positively correlated with the bone volume fraction, trabecular thickness, trabecular number, connectivity density and negatively correlated with the bone surface to volume ratio and trabecular separation. This study demonstrates that stochastic assessment of the inhomogeneity of bone mineral density from routine clinical DXA scans of human lumbar vertebrae may have the potential to serve as a valuable clinical tool in enhancing the prediction of risks for osteoporotic fractures in the spine. The main advantage of using DXA scans is that it would be cost effective, since most hospitals already have DXA machines and there would be no need for purchasing new equipment.

CHAPTER ONE

INTRODUCTION

Spine fractures are the most common type of osteoporotic fractures and are a major concern in the health care of the elderly population. Therefore, early diagnosis of patients with high risk of osteoporotic fractures is essential. Osteoporosis is a skeletal disease in which loss of bone mass and deterioration of bone microarchitecture cause a reduction in bone stiffness and strength, thus resulting in an increased risk of fragility fractures [1].

1.1 Imaging modalities available in clinical applications and basic science research

Radiographs and DXA are two major modalities using two dimensional (2D) projection images for assessing bone fragility in the clinical setting. Conventional X-ray radiography offers higher resolution for diagnosis of fragility fractures, whereas DXA images have lower resolution but provide a better estimation of bone mineral density (BMD). Dual energy X-ray absorptiometry (DXA) is currently the clinical tool of first choice for measuring BMD and for making clinical decisions of osteoporosis patients due to its high precision, accuracy, efficiency, low radiation dose, accessible measurement sites, and low cost relative to other densitometry techniques. However, these techniques are not efficient in the diagnosis of patients with osteopenia. Persons with bone mineral density that is lower than normal peak density (usually T-scores range from -1 to -2.5) are osteopenia patients.

BMD is a measure of bone mass or quantity of bone. However, bone fragility is not only dependent on its quantity, but also its quality. Bone quality is defined as the totality of features and characteristics that influence a bone's ability to resist fracture [2]. In recent years, advanced imaging modalities have been explored to assess bone quality using

other contributing factors, such as microarchitecture of trabecular bone, mineralization, microdamage and bone remodeling rates. The high resolution images, obtained from most common 3D imaging modalities such as quantitative computed tomography (QCT) and magnetic resonance imaging (MRI) could be directly used to assess the 3D microarchitecture of trabecular bone. One of the most promising 3D imaging techniques is high resolution peripheral quantitative computed tomography (HR-pQCT, also known as Micro-CT technique). However, the general public has limited access to these facilities, with affordability being a major concern. Moreover, these are still a high-end research tool rather than a diagnostic tool for clinical applications [2].

1.2 Various imaging techniques to enhance the prediction of bone fractures from 2D-projection images

Fractal texture analysis, a useful image processing technique, has been widely applied to high resolution 2D radiography images in both clinical and *in-vitro* studies [3-12]. This technique can be used to extract the hidden geometric and microstructural features of bone from the existing 2D projection images. Although texture analysis of high resolution radiography images has been performed to identify the parameters that are correlated with microarchitecture parameters of trabecular bone, it has rarely been applied to 2D projection images of DXA scans. The reason is that fractal texture analyses requires a large surface of projection and distinguishable textures whereas DXA images do not satisfy such requirements due to their low resolution.

Finite element analysis, is a technique used to extract stiffness and strength of the bone from DXA scans. This technique can be used to generate a 3D proximal femur shape from 2D radiographic images and used to construct the 3D finite element models [13]. The limitation of this technique is that it is only validated in *ex-vivo* studies and its application to routine clinical DXA images is not yet confirmed [13].

Topological analysis is another technique that has been applied to 2D DXA images to extract topological parameters. In a clinical study, the topological parameter based on the Minkowski function, can differentiate 30 postmenopausal women with and without hip

fractures [14]. However, the physical meaning of the topological parameter is irrelevant to bone strength.

Trabecular bone score (TBS) is a new parameter which can be extensively used in clinical situations [15]. The value of TBS is calculated as the slope at the origin of the log-log representation of the experimental variogram of grayscale values of DXA images [16-18]. In *ex-vivo* studies, TBS has been found a correlation with microarchitecture parameters of trabecular bone [15, 18, 19]. In retrospective case control studies, TBS has been found to complement BMD measured from DXA scans for postmenopausal women with hip fractures [17, 20, 21]. One of the limitations of TBS is that, the physical meaning of TBS is still unclear. TBS uses grayscale values and the use of grayscale values does not characterize the exact distribution of bone mineral density. Since TBS is defined as the initial slope of the log-log representation of the experimental variogram, it reflects only the initial trend, rather than a global measure of bone quality.

In the current study, a novel stochastic method has been used to describe the spatial variation of bone properties by quantifying the map of BMD derived from DXA scans. In this method, a theoretical semi-variogram model was fitted over the experimental variogram to evaluate the stochastic parameters. These stochastic parameters can describe the global trend of the experimental variograms and measure bone quality.

1.3 Objective and framework

This thesis investigates the relationship between stochastic parameters of BMD maps of DXA scans and microarchitecture parameters of Micro-CT images. 2D images of vertebrae are obtained using a DXA machine. 3D images of vertebrae are obtained using Micro-CT machine. Stochastic parameters of BMD maps were calculated using MATLAB (Mathworks, Natick, MA, USA). Microarchitecture parameters of trabecular bone were calculated using the *ImageJ* and *Microview* software. Statistical analysis of stochastic and microarchitecture parameters were performed using SPSS (IBM, Armonk, NY) [22] and Excel (Microsoft Office, Windows 8).

1.4 Organization of thesis

This thesis is divided into six chapters. Chapter 2 describes previous studies which are related to the current study. Chapter 3 explains the technical terms (variogram, stochastic and microarchitecture parameters) and imaging modalities (DXA and Micro-CT) which are used in our current study. Chapter 4 describes methods and experimental procedures to estimate stochastic and microarchitecture parameters. Chapter 5 lists and analyzes the results of statistical analysis of stochastic and microarchitecture parameters. Chapter 6 consists of conclusions and discussion.

CHAPTER TWO

PAST WORK

Texture analysis, a useful imaging technique which has been successfully applied to X-ray radiographs of iliac bone is correlated with bone micro-CT *in-vitro* study [23]. In this study, the anterosuperior part of the iliac bone was removed from 24 cadavers subjects (14 women and 10 men) [23]. Large samples were prepared consisting of the crest and a strip of bone approximately 3 cm wide and 5cm long. 2D projection images of the samples were obtained using micro-CT (Skyscan 1072) and 3D reconstructed models were obtained using surface rendering algorithms from the stack of 2D projection images. Microarchitecture parameters such as bone volume fraction (BV/TV), trabecular thickness (Tb.Th), trabecular separation (Tb.Sp), structure model index (SMI), trabecular number (Tb.N), trabecular bone pattern factor (Tb.Pf), absolute bone volume (C.BV/C.TV) were determined. A projection image was selected from stack of images and it was trimmed 2cm under the top of the iliac crest to perform texture analysis. Texture analysis was performed using various techniques such as skeletonization, run-length distribution, fractal analysis (skyscrapers, blanket). Simple and multiple linear regression analysis was performed between the data obtained from texture analysis of 2D projection images and microarchitecture parameters of 3D reconstructed volumes. A good correlation was found between bone volume fraction and absolute bone volume. structure model index and trabecular separation were negatively correlated with skeletonization parameters. Trabecular thicknes and trabecular number were positively correlated with several fractal dimensions and three groups of texture parameters respectively [23]. This study concludes that X-ray texture analysis seems to be suitable approach for 2D bone microarchitecture assessment due to a good correlation between texture analysis of X-ray radiographs and 3D bone microarchitecture assessed by micro-CT [23]. In another *in-vitro* study, texture analysis of bone is correlated with 3D microarchitecture and mechanical properties of trabecular bone in osteoporotic femurs

[24]. In this study, a total of 31 bone cores were used, which are obtained from 8 femoral heads of osteoporotic patients [24]. A high resolution X-ray device (BMA^{TM}) was used to obtain digitized anterior-posterior radiographs of these bone samples. Texture parameters were obtained such as fractal dimension H_{mean} , co-occurrence matrix, and run-length matrix [24]. High resolution micro-CT tomography operated in the cone beam method was used to image trabecular bone with a resolution of 20 μm . 3D microarchitecture parameters such as bone volume fraction (%), trabecular thickness (mm), trabecular number (1/mm), trabecular separation (mm) were measured. Uniaxial compression tests to failure were performed to estimate failure load and apparent modulus of bone samples. After performing statistical analysis, the fractal parameter H_{mean} demonstrated significant correlations with failure load ($r^2=0.84$) and apparent modulus ($r^2=0.71$). Bone volume fraction and trabecular thickness were also markedly correlated with failure load ($r^2=0.85$ and $r^2=0.72$ respectively) and apparent modulus ($r^2=0.72$ and $r^2=0.64$ respectively) [24]. The fractal parameter H_{mean} was also significantly correlated with bone volume fraction and trabecular thickness.

In a similar *in-vitro* study, radiographic texture analysis is correlated with 3D microarchitecture in the femoral head, and improves the estimation of femoral neck fracture risk when combined with bone mineral density [25]. In this study, 25 human femoral heads were obtained from 13 osteoporotic patients and 12 osteoarthritis patients. Univariate analysis showed that fractal parameter H_{mean} was correlated with 3D microarchitecture parameters : bone volume fraction, trabecular number, trabecular separation, and fractal dimension. In the same way, bone mineral density measured in contralateral femur of total hip and femoral neck were correlated with 3D microarchitecture parameters [25].

These two *vitro* studies [24, 25], texture analysis of femoral head have several limitations. First, the group of specimens was very small. Second, the results of these studies are based on evaluation of femoral head specimens, their generalization to the analysis of entire bones *ex-vivo* or *in-vivo* was limited [25]. Third, trabecular bone analysis was restricted to the femoral head in the two *vitro* studies. Finally, it is important

to recognize that 2D texture parameters do not provide true quantitative measurements of the physical bone structure. The two studies on texture analysis of femurs concluded that radiographic texture analysis is a suitable approach for trabecular microarchitecture assessment [24, 25].

In one study, microstructural parameters of bone evaluated using HR-pQCT were correlated with the DXA-derived cortical index and the trabecular bone score for randomly selected postmenopausal women [26]. In total, 72 women (N=69 white women) subjects were used in this study [26]. Bone mineral density was measured at the lumbar spine (L1-L4), femoral neck, total hip, distal radius, and at the two customized sub regions of the distal tibia using DXA (Hologic Discovery C^{TM}). The DXA derived cortical thickness (Ct.Th) was calculated from the DICOM images of the DXA scan at the distal tibia [26]. A new parameter cortical index for diaphyseal bone strength (CI) was defined as the product of a material (aBMD) and a structure component (pMOI). The dimensionless TBS of lumbar vertebrae (L1-L4) were calculated. After scanning distal tibia using HR-pQCT, bone morphological parameters such as volumetric bone mineral density (vBMD), bone volume fraction, trabecular bone mineral density (Tb.BMD), trabecular thickness, trabecular number, trabecular separation, inhomogeneity of trabecular network (Tb.I/N.SD), connectivity density, cortical bone density (Ct.BMD) and cortical thickness were evaluated [26]. From statistical analysis, a significant correlation was found between CI measured at tibia by DXA and HR-pQCT. Trabecular bone score was also significantly correlated with the bone volume fraction, trabecular bone mineral density, trabecular number, connectivity density, and negatively correlated with trabecular separation and inhomogeneity [26]. There was no correlation found between trabecular bone score and the trabecular thickness, total volumetric bone mineral density, cortical bone density and cortical thickness of different skeletal sites. The limitations of this study are that, all subjects are healthy postmenopausal women and only one skeletal region was considered. This study has concluded that microstructural parameters of bone assessed by the 3D technique were predictable through information deducted from regular 2D DXA scans [26].

In another study, a significant correlation was established between trabecular bone score of 2D projection images and 3D microarchitecture of different anatomical sites [15]. In this study, 57 human cadaver bone pieces (13 lumbar spine samples, 7 thoracic spine samples, 17 femoral neck samples and 3 distal radius samples) were used. These samples were scanned using HR-pQCT (eXplore Locus, GE HealthCare), with a resolution of 93 μm [15]. The 3D microarchitecture of trabecular bone was characterized in terms of bone volume fraction, stereological parameters based upon the parallel plate model, and model independent parameters based upon porous material characterization algorithms. Stereological parameters, trabecular thickness (mm), trabecular separation (mm), trabecular number (mm^{-1}) of all above mentioned samples were calculated using advanced Bone analysis *plugin* in Micro View software [15]. Model independent parameter, mean solid thickness (mm) was calculated using a chord length distribution method. The experimental variogram was calculated by averaging the squared difference of gray scale values of 2D projection image which is obtained from HR-pQCT [15]. Trabecular bone score was evaluated as the slope at the origin of the log-log representation of experimental variogram. High correlations were found between parallel plate model-based parameters and model-independent parameters after performing statistical analysis [15]. For spine samples, trabecular bone score was significantly correlated with trabecular number ($r^2 = -0.84$). In the set of femoral neck samples, more significant correlation was found between trabecular bone score and trabecular separation ($r^2 = 0.62$). Among distal radius samples, high correlation was obtained between trabecular bone score and trabecular thickness ($r^2 = 0.83$). From the stepwise multiple linear regression analysis, it is observed that for spine samples, trabecular bone score was assessed as a function of trabecular thickness and trabecular number; for femoral neck samples, as a function of trabecular thickness and trabecular separation; for distal radius samples, as a function of trabecular thickness and trabecular number [15]. This study concludes that TBS is a powerful measure to characterize the trabecular bone microarchitecture and it is an effective and efficient solution to apply to clinical DXA images [15].

In another *ex-vivo* study, trabecular bone score evaluated from DXA images of lumbar vertebrae was associated with microarchitecture parameters and with vertebral mechanical behavior [19]. In this study, 16 lumbar vertebrae specimens (L3) were used, which includes 7 men and 9 women [19]. These vertebrae were scanned using DXA (Delphi W, Hologic) to measure anteroposterior and lateral vertebral area (Ap. Area and Lat. Area, in cm^2), anteroposterior and lateral bone mineral content (Ap. BMC and Lat. BMC, in gram), and anteroposterior and lateral bone mineral density (Ap. BMD and Lat. BMD, in gram/cm^2) [19]. The TBS was calculated using *TBS inSight* software from anteroposterior DXA images of vertebrae. After removing soft tissue and posterior elements from individual vertebra, it was scanned using micro-CT (Skyscan 1076) and obtained 3D images of lumbar vertebra. Trabecular bone volume per tissue volume (%), trabecular thickness (mm), degree of anisotropy (#), and structure model index were measured from micro-CT images of lumbar vertebra (L3) [19]. The failure load (Newton) and compressive stiffness (Newton/mm) were measured from load displacement data, which is obtained from quasi-static uniaxial compressive testing. Statistical analysis was performed between data obtained from DXA images and data obtained from micro-CT images. Trabecular bone score was significantly correlated with trabecular bone volume fraction and structure model index ($r^2 = 0.58$ and $r^2 = -0.62$) but not associated with bone mineral content, bone mineral density, anterior-posterior and lateral area of specimen. A good correlation was found between trabecular bone score and stiffness. Bone mass parameters such as anterior-posterior bone mineral content, lateral bone mineral density and structure model index were significantly correlated with mechanical behavior [19]. When BMD is combined with TBS in stepwise linear regression analysis, this combination was failed to increase the fracture prediction. One limitation of this study is that the number of specimens were small and all specimens were collected from older individuals with low bone mass. So, the results of this study might not be representative of the normal population. Finally, this study concluded that TBS extracted from DXA images reflects trabecular bone microarchitecture and is an independent predictor of vertebral mechanical behavior [19].

In one previous study, biomechanical properties and microarchitecture parameters of trabecular bone were correlated with stochastic measures of 2D projection images [27].

In this study, 15 cylindrical specimens of trabecular bone which are cored from the proximal tibias of 6 male human cadavers were used [27]. HR-pQCT was used to scan these trabecular bone samples with a resolution of 50 μm . Microarchitecture parameters (BV/TV, BS/BV, Tb.Th, Tb.N, Tb.Sp) were calculated from 3D micro-CT images using stereological principles. Ultimate strength and elastic modulus of the trabecular bone samples were evaluated from stress-strain curves [27]. Ultimate strength was evaluated as maximum stress sustained by the sample during compression test and elastic modulus was evaluated as the slope of the linear region of stress-strain curve. Spatial variation of a BMD of 2D projection images was characterized by experimental variograms. Stochastic measures such as correlation length (L), sill variance (C), nugget variance (C_0) were evaluated by fitting theoretical exponential models over experimental variogram [27].

Simple linear regression analyses were performed between stochastic measures of 2D projection images and microarchitecture parameters, mechanical properties of trabecular bone from human tibias. A significant positive correlation was observed between sill variance and elastic modulus ($r^2=0.81$) and between sill variance and ultimate strength ($r^2=0.82$) of trabecular bone [27]. Linear regression analysis indicated that sill variance is significantly correlated with bone volume fraction ($r^2=0.56$), bone surface to volume ratio ($r^2=0.54$), trabecular thickness ($r^2=0.54$), trabecular number ($r^2=0.48$), trabecular separation ($r^2=0.50$), and anisotropy ($r^2=0.37$). No relationships were found between correlation length and biomechanical as well as microarchitecture parameters of trabecular bone. This study has several limitations; areal bone mineral density was represented with gray scale values in 2D projection images; Both high density and low density trabecular bone samples were used; 2D projection images of micro-CT scans with a resolution of 300 μm may not be exactly the same as DXA images; Finally, the cylindrical specimens do not represent irregular bone shapes in clinical applications. This study concludes that sill variance has good correlation with microarchitecture parameters and biomechanical properties of bone [27]. So, this stochastic assessment of BMD can be extended to 2D projection images obtained from DXA to improve the prediction of bone fragility.

Table 2.1 Summary of selected previous studies

Author, year	Method/Parameter	Significance of study
P. Guggenbuhl, 2006 [23]	Texture analysis of X-ray radiographs of iliac bone	Tb.Th and Tb.N were positively correlated with texture parameters
Thomas Le Corroller, 2013 [24]	Texture analysis of X-ray radiographs of osteoporotic femurs	Fractal parameter H_{mean} was significantly correlated with BV/TV, Tb.N, Tb.Sp and FD
Matthieu Ollivier, 2013 [25]	Texture analysis of X-ray radiographs of femoral head	Fractal parameter H_{mean} was correlated with failure load, apparent modulus, BV/TV and Tb.Th
Albrecht W. Popp, 2014 [26]	DXA derived cortical index and TBS in Postmenopausal women	TBS was significantly correlated with Tb.BMD, BV/TV, Tb.N, Conn.D
Laurent Pothuad, 2008 [15]	TBS evaluation of human cadaver bone specimens	TBS was correlated with Tb.N, Tb.Sp and Tb.Th of spine, femoral neck and distal radius samples respectively
J. P. Roux, 2013 [19]	TBS calculation of DXA image of lumbar vertebrae	TBS was significantly correlated with Tb.BV/TV, SMI and stiffness
Xuanliang N. Dong, 2013 [27]	Stochastic assessment of 2D projection images of trabecular bone	Sill variance was correlated with elastic modulus, ultimate strength, BV/TV, BS/BV, Tb.Th, Tb.N, Tb.Sp

In the current study, stochastic parameters were calculated by fitting theoretical model onto the experimental variogram of BMD map of DXA scans. Microarchitecture parameters were measured within the vertebral body from 3D images of vertebrae. In statistical analysis, stochastic parameters of BMD map of vertebrae are significantly correlated with microarchitecture parameters of vertebral body.

CHAPTER THREE

TECHNICAL BACKGROUND

This chapter describes the technical terms that are used in this study, which mainly concentrate on medical imaging of bones. Medical images includes two dimensional images (2D) as well as three dimensional images (3D). The imaging modalities that are available in clinical applications are capable of producing only 2D images with low resolution. Imaging modalities that are available in basic science research such as Micro-CT are capable of producing 3D images with high resolution. The techniques which have been implemented in this study to obtain the required parameters are described in following sections.

3.1 Dual-Energy X-ray absorptiometry (DXA)

One of the most important application of DXA is measuring BMD that can be used to assess the possibility of bone fractures. DXA has advantages of higher precision, shorter scanning times, low radiation dose, and improved calibration stability in the clinical environment. Because of these advantages DXA has seen widespread use in prospective clinical trials of new therapies for osteoporosis [28, 29]. Usually the spine and hip are the two sites chosen for BMD measurement, because these are the most common sites for osteoporotic fractures. The fundamental physical principle behind DXA is the measurement of the transmission through the body of x-rays with high and low photon energies [30].

The first generation of DXA scanners used a pencil beam technique and the new generation DXA scanners use a fan beam technique [30]. Fan beam technique is implemented by performing a single sweep across the patients instead of the two dimensional raster scan required by pencil beam geometry. The advantages of fan beam

systems are higher image resolution and shorter scan times compared to pencil beam systems. In our study, new generation DXA (QDR Discovery A) with fan beam mode was used to obtain the scans of vertebrae. When a DXA scan is analyzed the basic raw data is processed to create a pixel-by-pixel map of BMD over the entire scan.



Figure 3.1 Dual energy X-ray absorptiometry machine

3.2 Micro-computed tomography (Micro-CT)

The major application of Micro-CT is to scan a small specimen and generate high-resolution 3D images. Small specimens may include human vertebrae separated from cadavers spine. Three-dimensional (3D) microarchitecture of bone can also be described using Micro-CT images. Due to its high resolution, Micro-CT can obtain precise 3D images at the micro-level of trabecular bone structure. Although high resolution is achievable using Micro-CT, scanning large specimens such as a whole vertebral body may require use of spatial resolution corresponding to a voxel size greater than 100 μm . Because 100 μm is in the order of typical trabecular thickness, partial volume effects will cause errors when computing the stereological parameters for trabecular bone. Micro-CT machine has its major applications in research areas only, because of its high radiation. Using Micro-CT the specimen can be scanned at one voxel size and the raw data reconstructed at a different voxel size. Voxel is defined as a volumetric pixel of the object in a 3D image similar to a pixel of an object in a 2D image.



Figure 3.2 Micro computed tomography machine

3.3 Experimental variogram

The variogram is a descriptive statistic that can be used to characterize the spatial variation of bone mineral density over the different regions of bone [31, 32]. A semi-variance, $\gamma(\mathbf{h})$, is defined as the half of the expected squared differences of bone mineral density between any two data locations with a lag distance of \mathbf{h} .

$$\gamma(\mathbf{h}) = \frac{1}{2} E[\{Z(\mathbf{x}) - Z(\mathbf{x} + \mathbf{h})\}^2] \quad (3.1)$$

where $Z(\mathbf{x})$ is a function to describe the random field of bone mineral density; Both \mathbf{x} and \mathbf{h} are vectors; \mathbf{x} is the spatial coordinates of the data location. Lag distance, \mathbf{h} , represents the Euclidean distance and direction between any two data locations.

The experimental variogram is calculated as an average of semi-variance values at different locations that have the same value of lag distance (\mathbf{h}).

$$\hat{\gamma}(h) = \frac{1}{2m(h)} \sum_{i=1}^{m(h)} E[\{Z(\mathbf{x}_i) - Z(\mathbf{x}_i + h)\}^2] \quad (3.2)$$

where $m(\mathbf{h})$ is the number of data pairs for the observations with a lag distance of \mathbf{h} .

The variogram model is chosen from a set of mathematical functions that describe spatial relationships. The appropriate theoretical model is chosen by matching the shape of the curve of the experimental variogram to the shape of the curve of the mathematical function. The function must therefore be mathematically defined for all real lag distances.

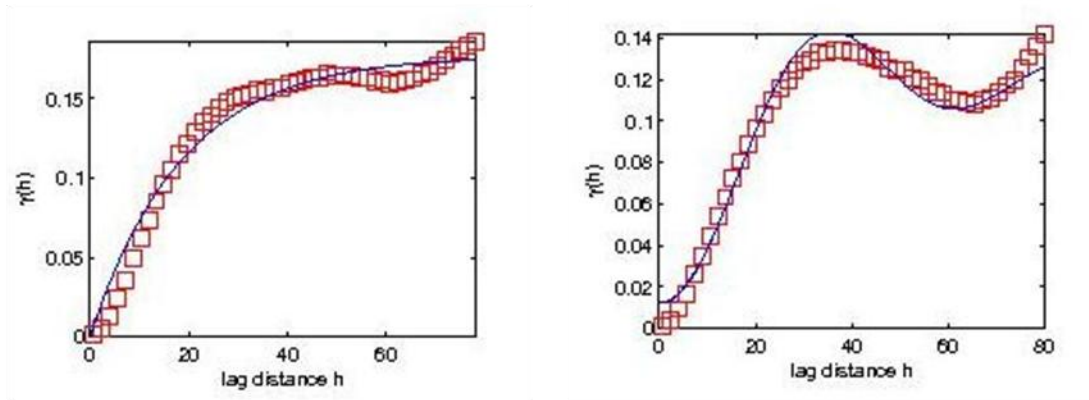


Figure 3.3 Theoretical exponential model (left) and hole-effect model (right) fitted over the experimental variogram of the bone mineral density map

There are a few principal features that a function must be able to represent. These include:

- (a) a monotonic increase with increasing lag distance from the ordinate
- (b) a constant maximum or asymptote, or 'sill'
- (c) a positive intercept on the ordinate, or 'nugget'
- (d) periodic fluctuation, or a 'hole' and anisotropy.

Stochastic parameters (correlation length, sill and nugget variance) are described below

3.3.1 Correlation length or range (L)

The lag distance at which semi-variogram reaches the sill value. Correlation length describes the degree of smoothness or roughness in the BMD map. A relatively large correlation length implies a smooth variation, whereas a small correlation length corresponded to rapid variations of the bone mineral density over the spatial domain.

3.3.2 Sill variance (C)

The sill variance is defined as the limit of the experimental variogram tending to infinity lag distances. It can be used to refer to the "amplitude" of certain component of the semi-variogram. The sill of the variogram represents the variance of the BMD map.

3.3.3 Nugget variance (C_0)

According to theory, the semi-variogram value at the origin should be zero. If it is significantly different from zero for lag distance close to zero, then this semi-variogram value is referred to as nugget variance. It represents the sum of noise in a image and measurement errors of calculations.

Table 3.1 Stochastic parameters of experimental variogram

Parameter	Formula	Meaning
Correlation length	L	Lag distance at which semi-variogram reaches sill value
Sill variance	C	Maximum value of the semi-variogram
Nugget variance	C_0	Sum of noise in a image and measurement errors

3.4 Microarchitecture parameters of trabecular bone

The geometric and spatial properties of trabeculae in trabecular bone are collectively known as the trabecular bone architecture. Trabecular bone is a highly porous or cellular form of bone. Trabeculae is a microscopic tissue element in the form of a small beam, strut or rod, generally having a mechanical function. Trabecular bone microarchitecture resembles the connectivity of rods and plates in 3D space. This structure of trabecular bone can be described by microarchitecture parameters such as connectivity and structural model index and is discussed in following sections.

3.4.1 Bone volume fraction (BV/TV)

The bone volume fraction, is one of the fundamental architectural properties of trabecular bone, and it is defined as the trabecular bone volume per reference volume. It has

negative relationship with porosity. A large bone volume fraction is indicative of high bone strength. For a specimen,

$$\frac{Bv}{Tv} = \frac{\text{Trabecular bone volume}}{\text{trabecular bone volume} + \text{marrow space volume}} \quad (3.3)$$

3.4.2 Trabecular thickness (Tb.Th)

Trabecular thickness is defined as average thickness of trabeculae in trabecular bone. Trabecular thickness decreases with increasing age. Decreasing trabecular thickness leads to reduces the bone strength.

3.4.3 Trabecular separation (Tb.Sp)

Trabecular separation is essentially the thickness of the spaces between two trabeculae. It measures marrow space between two trabeculae. Trabecular separation increases with increasing age. High trabecular separation represents less bone strength.

3.4.4 Trabecular number (Tb.N)

Trabecular number implies the number of traversals across a trabecular or solid structure made per unit length on a linear path through a trabecular bone region. Trabecular number decreases with increasing age. High trabecular number is indicative of high bone strength.

3.4.5 Connectivity density (Conn.Dn)

Connectivity reports the number of redundant trabeculae in trabecular bone. A redundant trabeculae is a trabeculae that may be cut without increasing the number of separate parts of the bone structure. Increasing the number of unconnected trabeculae leads to the reduction of bone strength. The central parameter is the Euler Number χ , also known as Euler characteristic [33]. Euler number in 3D bone structure with β_0 separate bone particles, β_1 redundant connections, β_2 fully enclosed marrow cavities isolated from the main marrow space is given as,

$$\chi = \beta_0 - \beta_1 + \beta_2 \quad (3.4)$$

3.4.6 Bone surface to volume ratio (BS/BV)

The surface to volume ratio characterizes the rate of bone turnover because bone desorption and formation can only occur on bone surfaces. A large bone surface to volume ratio is indicative of high rate of bone turnover.

3.4.7 Structure model index (SMI)

The structure model index is a factor that characterizes the plate or rod like geometry of trabecular structures. Typical values of structure model index lie between 0 and 3. Zero specifies purely plate shaped trabeculae and three specifies purely rod like trabeculae. Structure model index can be calculated as follows

$$SMI = 6 \cdot \left(\frac{B\bar{S} \cdot BV}{BS^2} \right) \quad (3.5)$$

where BS and $B\bar{S}$ stands for the trabecular surface area before and after dilation, BV being the initial undilated volume of the trabeculae.

3.4.8 Trabecular bone pattern factor (Tb. P_f)

Trabecular bone pattern factor is an index of connectivity based on the relative concavity or convexity of the total trabecular surface. Trabecular bone pattern factor can be calculated by comparing area and volume of trabeculae before and after dilation.

$$Tb.P_f = \frac{(BS_1 - BS_2)}{(BV_1 - BV_2)} \quad (3.6)$$

where the subscript numbers 1 and 2 represent before and after image dilation.

3.4.9 Degree of anisotropy (DA)

Degree of anisotropy is a measure of orientation of trabeculae in trabecular bone. Trabecular bone varies its orientation depending on mechanical load and it can become anisotropic. Mean intercept length (MIL) method can be used to determine degree of anisotropy.

The mathematical equation of degree of anisotropy is given as,

$$DA = 1 - \left(\frac{MIL1}{MIL2} \right) \quad (3.7)$$

Where MIL1 and MIL2 stands for minimum and maximum mean intercept lengths of trabeculae respectively.

Table 3.2 Microarchitecture parameters of trabecular bone

Parameter	Formula	Meaning
Bone volume fraction	BV/TV	Trabecular bone volume per reference volume
Trabecular Thickness	Tb.Th	Average thickness of trabeculae
Trabecular Separation	Tb.Sp	Thickness of marrow space between two trabeculae
Trabecular Number	Tb.N	Number of trabeculae in unit length
Connectivity Density	Conn.Dn	Number of unconnected trabeculae
Bone surface to volume ratio	BS/BV	Rate of bone turnover
Structure Model Index	SMI	Characterizes the plate or rod like geometry of trabecular structures
Trabecular bone pattern factor	Tb. P_f	Index of connectivity based on the relative concavity or convexity
Degree of Anisotropy	DA	Orientation of trabeculae

CHAPTER FOUR

METHODS AND EXPERIMENTAL PROCEDURES

In this study, eighteen fresh human lumbar vertebrae were obtained from five tissue donors (4 males and 1 female; 70.0 ± 10.4 years old; range: 57 to 81 years old) through The National Disease Research Interchange (NDRI, Philadelphia, PA). Soft tissue was removed over cadavers spine and all lumbar vertebrae were dissected out of it. The posterior elements were intact and remained with the human vertebrae. The absence of prevalent fracture or significant bone disease (i.e, bone metastasis, Paget's disease of the bone, major osteoarthritis) was assessed using DXA. The vertebral specimens were wrapped with gauze and stored at -25°C until DXA image acquisition and Micro-CT image acquisition was performed.

4.1 DXA image acquisition

Two-dimensional images of specimens were obtained using Dual energy X-ray absorptiometry (Hologic QDR Discovery W, Bedford, MA) operating in a fan beam mode. Before scanning of vertebrae, a quality control (QC) test was performed using the manufacturer supplied spine phantom. Long term coefficient of variation was observed. One of the major benefits of instigating a QC protocol involving the regular scanning of a phantom is that it may allow the early identification of changes in instrument performance prior to instrument malfunction, although, not all malfunctions will affect BMD data. The procedure to acquire the DXA images is described below:

- Collect all the required items such as one small plastic container, one large plastic container, a pair of Plexiglas wedges, a small foam box for storage of human vertebra and reusable ice packs to perform the DXA scans of vertebrae.

- Fill up the small container with water to simulate the soft tissue and place in a large container.
- Place vertebra under water in Posterior Anterior (PA) direction (Figure 4.1). Two Plexiglas wedges were used to stand the vertebra in PA-direction. Adjust positions of glass wedges to keep the vertebra in perfect vertical position.
- Select AP-Lumbar spine mode on the DXA machine to scan the vertebra (Figure 4.1). The position of the specimen was adjusted without disturbing the equipment on the DXA machine by selecting an option called *Reposition scan*.



Figure 4.1 Gray scale image of DXA scan of lumbar vertebra (L3) in PA-direction

- Analyze DXA scan according to standard lumbar spine protocol described by Hologic to obtain the bone mineral content (g), bone mineral density (g/cm^2) and area (cm^2) of specimen in PA-direction.
- The raw data files (i.e, R files) and screen captured images of DXA scan of a specimen were copied into flash drive to create a BMD map.

- Once required scans of specimen were completed, the specimen should be stored in a freezer maintaining at sufficient lower temperatures to obtain the Micro-CT images.

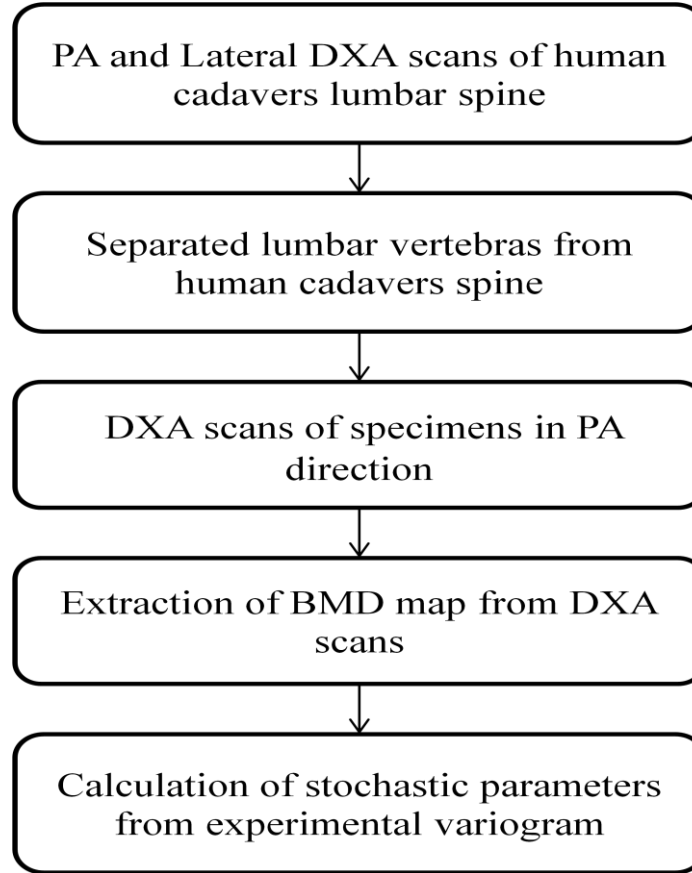


Figure 4.2 Sequence of steps to obtain the stochastic parameters of vertebrae DXA scans

4.2 BMD map extraction from DXA scans

After completion of DXA scans of vertebrae, raw data files (i.e., R files in Hologic densitometers) are extracted from the DXA machine. Code was developed in MATLAB (Mathworks, Natick, MA, USA) software to obtain the BMD map (Figure 4.3) of DXA scans. The raw data files of DXA consist of low and high energy values of air, bone and soft tissue respectively. The BMD map of vertebrae was obtained by directly operating on the transmission measurements of low-energy and high-energy X-ray beams [30, 34, 35]. There were two reasons for extracting the BMD map straightly from the raw data, rather than using the DXA image provided by the densitometer. First, grayscale values in the DXA image were not the exact value of bone mineral density of human vertebrae.

Second, grayscale values in DXA images could be easily affected by varying the brightness and the contrast of these DXA images.



Figure 4.3 BMD map of lumbar vertebra (L3) in PA-direction

4.3 Stochastic assessment of BMD map

Stochastic assessment of inhomogeneity or BMD distribution can be described by experimental variograms, which are widely used in geosciences [31, 32]. In this study, the spatial variation of BMD map from DXA scans was evaluated using a variogram, which could be expressed in two parameters: semi-variance and lag. Current techniques for quantifying bone heterogeneity consist of descriptive statistics such as mean and standard deviation. However, these parameters do not describe the spatial variations of bone properties. The stochastic method allows us to assess the quality of bone.

The semi-variance $\gamma(\mathbf{h})$ was defined as half of the expected squared difference between any paired data values $\{z(\mathbf{x}), z(\mathbf{x}+\mathbf{h})\}$:

$$\gamma(h) = \frac{1}{2} E[\{z(x) - z(x+h)\}]^2 \quad (4.1)$$

where \mathbf{z} is a random function of the indentation modulus of bone that varies continuously in space, \mathbf{x} denotes the spatial coordinates of locations and \mathbf{h} , also known as lag, is a vector representing the Euclidean distance and direction between any two data locations.

The experimental variogram for BMD map of vertebrae was computed as an average of semi-variance values at different locations that have the same value of lag:

$$\hat{\gamma}(h) = \frac{1}{2m(h)} \sum_{i=1}^{m(h)} \{z(x_i) - z(x_i+h)\}^2 \quad (4.2)$$

where $m(h)$ is the number of data pairs $\{z(x_i), z(x_i+h)\}$ for observations separated by h .

A hole-effect theoretical variogram model was fitted over the experimental variogram of BMD map obtained from DXA scans. The main reason for using hole-effect model is that the experimental variogram of the BMD map decreased from its maximum to a local minimum and then increased again, indicating fairly regular repetition in the process.

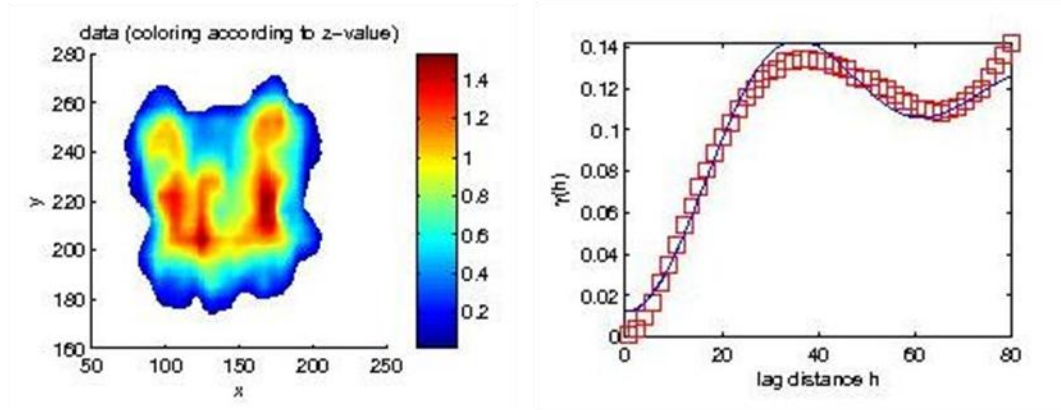


Figure 4.4 Color map of vertebra BMD map in PA-direction (left), hole-effect model is fitted over experimental variogram of BMD map (right)

The mathematical definition of hole effect model is given as

$$\gamma(h) = c(1 - \frac{\sin(h \pi / L)}{(h \pi / L)}) \quad (4.3)$$

where $\gamma(h)$ is the semi-variance as a function of lag (h), ' L ' is referred to as the correlation length and ' c ' is referred to as sill variance of BMD map.

4.4 Micro-CT image acquisition

Human lumbar vertebrae (N=18) were scanned using the GE Healthcare Explore Locus Micro-CT scanner at The University of Texas Health Science Center at Tyler (UTHSC) to obtain 3D images of trabecular bone. These Micro-CT scans were performed by following established procedures with a isotropic voxel size of 92 μm . This is the smallest available voxel size in this scanning system for the size of vertebrae used in this study.

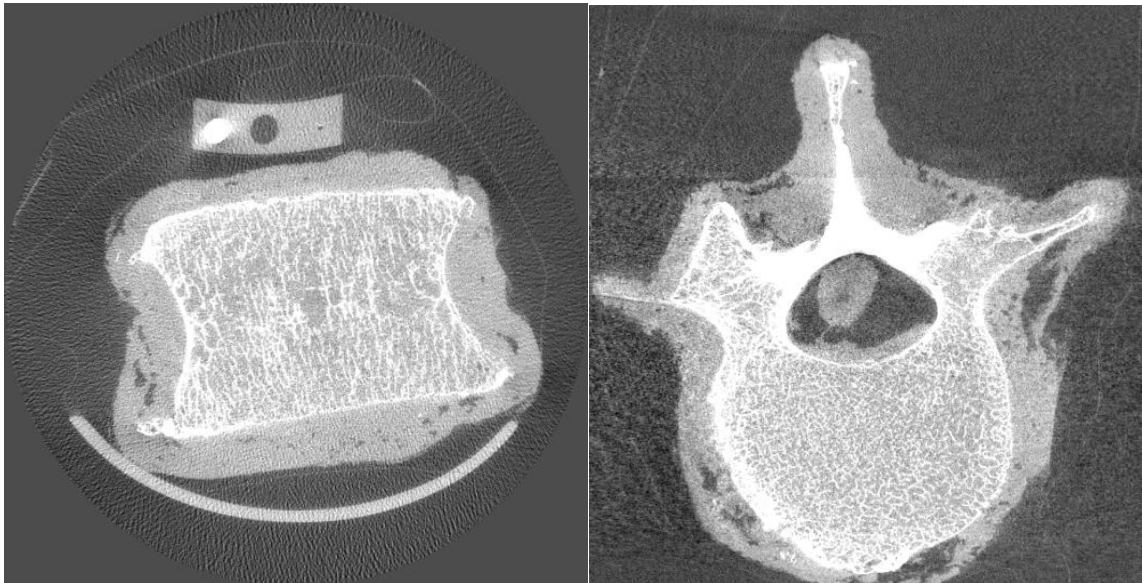


Figure 4.5 Gray scale images of a vertebral body obtained from μCT (a) Coronal cross-section (left side) (b) Axial cross-section (right side)

The attenuation values of micro-CT (gray levels) were scaled with a calibrated solid phantom and recorded in Hounsfield Units (HU). This low resolution scan of specimen took approximately 15 to 20 minutes. The stack of images were reconstructed based on specific algorithm with a reconstruction voxel size that is same as scanning voxel size, so that each data point of the reconstruction represented a sub-volume of the actual specimen. The reconstructed images can be displayed as a stack of gray scale images (Figure 4.5). The whole reconstruction process took approximately 45 minutes. The

reconstructed images were stored in an external hard drive to obtain the microarchitecture parameters. After completion of Micro-CT scans of vertebrae, specimens were stored in freezer at sufficient low temperature to perform mechanical testing.

4.5 Measuring microarchitecture parameters of trabecular bone

Bones are commonly imaged using computed tomographic (CT) and X-ray micro computed tomographic (μ CT) systems for research purposes, such as investigating trabecular and cortical changes in osteoporosis. Many of the scans were over 1GB, and the existing software could not process large datasets, required a per-machine launch fee, or did not implement the required features. We needed to open varied image formats from diverse instruments, then pre-process, analyze and visualize scans efficiently on several different computers, remote from scanning hardware. We took advantage of the existing functionality and flexible plugin architecture of the public domain image processing program *ImageJ* [36].

In this study, the *ImageJ* plugin *BoneJ* was used to obtain the threshold images. Threshold images obtained from *ImageJ* imported into *Microview* (GE Healthcare, London, ON, Canada) to calculate the microrarchitecture parameters of lumbar vertebrae.

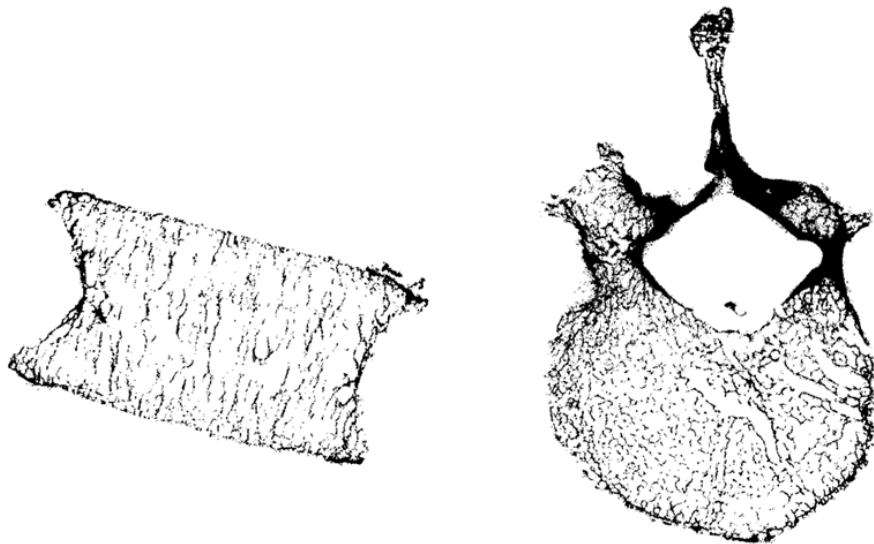


Figure 4.6 Binary images of a vertebra (a) Coronal cross-section (left side) (b) Axial cross-section (right side)

- Stitched image was opened using plugin *Input-Output* with option *Multi VFF Opener*. The stitched image consists of three volumes scanned in various regions of the whole vertebra.
- Converted stack of 16-bit images to stack of 8-bit images. Median filter with radius of two pixels was used to remove the noise in stack of gray scale images.
- Stack of threshold images were obtained by adjusting threshold value with a *threshold* option. Tube and phantom were removed from threshold images.
- Vertebral body separated from posterior elements. Threshold images were purified using plugin *BoneJ* with an option *purify*.
- After purification saved all the stack of images of vertebral body in a separated folder to convert the format of images.
- Imported the stack of threshold images (vertebral body) into *Microview* to measure microarchitecture parameters.
- Cylindrical region of interest (ROI) was used to measure microarchitecture parameters of vertebral body using *Bone analysis*. Maximum volume of vertebral body is covered without cortical shell using cylindrical ROI.

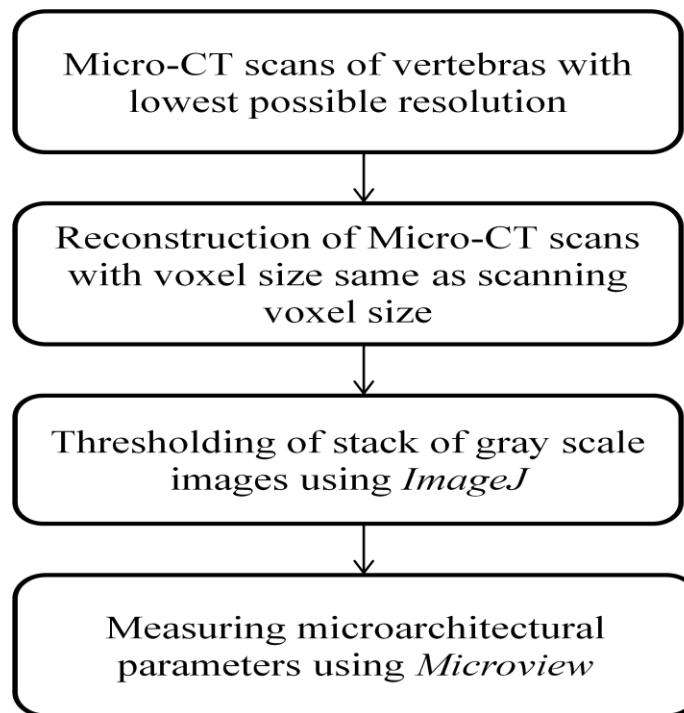


Figure 4.7 Sequence of steps to evaluate microarchitecture parameters of specimens

4.6 Statistical analysis

For statistical analyses, linear regression analysis and correlation test were used to model the relationship between stochastic parameters and microarchitecture parameters. Linear regression analysis was performed using Excel spread sheet (Microsoft Office, Windows-8). Bivariate correlation test was performed using SPSS (IBM, Armonk, NY).

4.6.1 Linear regression analysis

Main aim of linear regression analysis is to find the relationship between any two variables (ex: *sill variance* and *bone volume fraction*). Of the two variables included, one variable is considered to be an independent variable, and the other is considered to be a dependent variable. In linear regression analysis a straight line was fitted with slope and intercept for the two data sets.

Mathematical expression of a straight line obtained from linear regression analysis is given as

$$y = mx + c \quad (4.5)$$

where m represents slope of the line which could be positive or negative, c represents y-intercept, 'x' is a independent variable, 'y' is a dependent variable. The most common method used for fitting a straight line in linear regression is *least squares* method [37].

One other important parameter in linear regression analysis is coefficient of determination (R^2) which gives a percentage value. R^2 value explains how strong the given data sets are correlated. If the value of R^2 is more than 0.9, given data sets are strongly correlated, if it is around 0.5 given data sets are partially correlated and if it is less than 0.5 that considered as given data sets are weakly correlated.

In Excel sheet, the two data sets are selected and plotted (*scatter with only markers*). The equation of a fitted line and R^2 value is displayed on the plot using an option "*Add trend line*" (Display Equation on the chart and Display the R-squared value on the chart). The same procedure is repeated for remaining data sets to find the significant results.

4.6.2 Correlation test

The main purpose of correlation test is to determine whether there is a significant relationship between any two variables. Bivariate correlation test can be performed using Pearson's correlation (Parametric method) or Spearman's correlation (Non-Parametric method) in SPSS [22]. In our study Pearson's correlation test was performed to find the relationship between stochastic and microarchitecture parameters.

Correlation coefficient (r) of Pearson's test always lies between -1 and +1. If correlation coefficient is 0 that indicates there is no relationship between two variables. A correlation coefficient of +1 means that there is perfect positive correlation between two variables. In this case, as one variables increases, the second variable increases in exactly the same proportion. If correlation coefficient is -1 that represents perfect negative correlation between two variables. Perfect negative correlation or relationship means, as one variable increases, the second variable decreases in exactly the same proportion.

The mathematical expression of Pearson's correlation coefficient (r) is given as

$$r = \frac{\sum xy - N\bar{x}\bar{y}}{\sqrt{(\sum x^2 - N\bar{x}^2)(\sum y^2 - N\bar{y}^2)}} \quad (4.6)$$

where x , y are the two equal data sets. \bar{x} and \bar{y} are the average values of two data sets x and y respectively. N is the total number of data pairs.

One other important parameter in Pearson's correlation test is p -value to determine whether the correlation is statistically significant or not. The procedure to calculate or to estimate the p -value for correlation coefficient analysis is described in Appendix A.

Correlation is statistically significant if the p -value is less than 0.05 and it is represented by single asterisk (*) in SPSS. Correlation is statistically highly significant if the p -value is less than 0.01 and it is represented by double asterisk (**) in SPSS.

CHAPTER FIVE

RESULTS

In this study, a total of eighteen lumbar vertebrae which include L1 (N=4), L2 (N=4), L3 (N=4), L4 (N=4), L5 (N=2) are used. DXA, stochastic and microarchitecture parameters of all vertebrae and correlation analysis of these parameters were provided in this chapter.

5.1 Microarchitecture parameters calculated from micro-CT images

Microarchitecture parameters such as BV/TV, BS/BV (mm^2/mm^3), Tb.Th (mm), Tb.N (1/mm), Tb.Sp (mm), and Conn.Dn (mm^{-3}) were calculated from Micro-CT images of each vertebral body and tabulated below.

Table 5.1 Microarchitecture parameters of lumbar vertebral bodies

No	Specimen	BV/TV	BS/BV	Tb.Th	Tb.N	Tb.Sp	Conn.Dn
1	69099-L1	0.285078	8.167961	0.244859	1.149912	0.621719	1.29605
2	69099-L2	0.271276	8.533917	0.234359	1.157523	0.629555	1.33995
3	69099-L3	0.250239	8.906055	0.224566	1.114323	0.67284	1.2631
4	69099-L4	0.239621	8.734281	0.228983	1.046458	0.726622	1.08152
5	69099-L5	0.237176	8.761235	0.228278	1.038979	0.734205	1.14732
6	69111-L1	0.188431	9.276805	0.215591	0.874021	0.928546	0.77694
7	69111-L2	0.166298	9.765169	0.20481	0.811963	1.026773	0.7262
8	69111-L3	0.146029	10.03701	0.199263	0.732846	1.16528	0.58238
9	69111-L4	0.152348	9.675566	0.206706	0.737028	1.150094	0.63762
10	69111-L5	0.186262	9.042307	0.221182	0.842119	0.966298	0.79322
11	69013-L4	0.180221	8.95426	0.223357	0.806872	1.015997	0.63467
12	01595-L1	0.243544	8.071331	0.247791	0.982863	0.769645	0.93442
13	01595-L2	0.280634	7.414707	0.269734	1.04041	0.691425	1.00038
14	01595-L3	0.253995	7.741705	0.258341	0.983176	0.758771	0.87413
15	01854-L1	0.226677	8.602905	0.23248	0.975042	0.793117	1.02925
16	01854-L2	0.23002	7.840973	0.25507	0.90179	0.853835	0.85709
17	01854-L3	0.174049	10.00913	0.199817	0.87104	0.948236	0.78386
18	01854-L4	0.174745	9.886659	0.202293	0.863823	0.955351	0.82901

5.2 DXA and stochastic parameters of vertebrae

Stochastic parameters of DXA scans were evaluated by fitting hole-effect theoretical variogram model over the experimental variogram of the BMD map of vertebrae. DXA parameters, BMD calculated from raw data of DXA using MATLAB and stochastic parameters evaluated from variogram of BMD maps were tabulated below.

Table 5.2 DXA and stochastic parameters of vertebrae

No.	Specimen	DXA Area	DXA BMC	DXA BMD	BMD Calculated	Range	Sill	Nugget
1	69099-L1	16.38	15.01	0.916	0.70868	31.32	0.12093	0.025684
2	69099-L2	16.9	17.09	1.011	0.78269	23.454	0.13284	2.21E-02
3	69099-L3	19.41	19.31	0.995	0.78609	23.727	0.14239	2.25E-02
4	69099-L4	18.93	18.31	0.967	0.74913	31.33	0.1357	0.024199
5	69099-L5	20.02	18.47	0.923	0.72292	28.606	0.11096	0.020404
6	69111-L1	16.73	12.54	0.749	0.57211	28.838	0.07748	0.014037
7	69111-L2	17.35	15.51	0.894	0.68209	35.325	0.09474	0.02649
8	69111-L3	19.41	17.49	0.901	0.70322	24.972	0.10758	0.012175
9	69111-L4	20.94	19.3	0.921	0.73744	26.041	0.09151	0.019809
10	69111-L5	21.33	16.27	0.763	0.60319	27.959	0.07498	0.005679
11	69013-L4	18.59	17.65	0.949	0.71852	18.304	0.11961	1.20E-02
12	01595-L1	14.64	13.6	0.929	0.73244	30.709	0.11585	0.024873
13	01595-L2	15.6	15.47	0.992	0.75596	30.922	0.13332	0.029204
14	01595-L3	15.52	16.24	1.046	0.80205	30.359	0.15003	0.032893
15	01854-L1	14.92	14.15	0.948	0.75974	17.685	0.11159	1.22E-02
16	01854-L2	19.31	18.74	0.971	0.68216	25.495	0.11671	0.014152
17	01854-L3	17.86	19.45	1.089	0.87498	35.328	0.11492	0.040751
18	01854-L4	21.16	20.57	0.972	0.7731	26.924	0.1267	0.015612

Table 5.3 Descriptive statistics of DXA and stochastic parameters

Parameter	Mean \pm SD	Range
Area (cm^2)	18.05 \pm 2.15	14.64-21.33
BMC (g)	16.95 \pm 2.25	12.54-20.57
BMD (g/cm^2)	0.940 \pm 0.08	0.749-1.089
Range (mm)	27.62 \pm 4.90	17.68-35.32
Sill (g/cm^2) ²	0.115 \pm 0.02	0.074-0.150
Nugget (g/cm^2) ²	0.02 \pm 0.008	0.005-0.040

Table 5.4 Descriptive statistics of microarchitecture parameters

Parameter	Mean \pm SD	Range
BV/TV	0.215 \pm 0.045	0.146-0.285
BS/BV(mm ² /mm ³)	8.856 \pm 0.809	7.414-10.03
Tb.Th (mm)	0.227 \pm 0.021	0.199-0.269
Tb.N (1/mm)	0.940 \pm 0.133	0.732-1.157
Tb.Sp (mm)	0.856 \pm 0.170	0.621-1.165
Conn.Dn (mm ⁻³)	0.921 \pm 0.231	0.582-1.339

BV/TV- bone volume fraction, *BS/BV*- bone surface to volume ratio, *Tb.Th*- trabecular thickness, *Tb.N*- trabecular number, *Tb.Sp*- trabecular separation, *Conn.Dn*- connectivity density, *BMC*-bone mineral content, *BMD*-bone mineral density

5.3 Pearson correlation coefficient analysis of stochastic, microarchitecture and DXA parameters

Sill variance of hole-effect variogram model was significantly positively correlated with the bone volume fraction ($r=0.621$, $p=0.006$), trabecular thickness ($r=0.484$, $p=0.042$), trabecular number ($r=0.611$, $p=0.007$), connectivity density ($r=0.515$, $p=0.029$) and negatively correlated with bone surface to volume ratio ($r=-0.473$, $p=0.048$), trabecular separation ($r=-0.614$, $p=0.007$). Significant results of Pearson correlation coefficient analysis between stochastic and microarchitecture parameters were tabulated below.

Table 5.5 Pearson correlation coefficients between stochastic and microarchitecture parameters

	BV/TV	BS/BV	Tb.Th	Tb.N	Tb.Sp	Conn.Dn
Sill	0.621**	-0.473**	0.484*	0.611**	-0.614**	0.515*
BV/TV	1	-0.862**	0.845**	0.936**	-0.966**	0.858**
BS/BV	-0.862**	1	-0.996**	-0.637**	0.735**	-0.510**
Tb.Th	0.845**	-0.996**	1	0.608**	-0.709**	0.472*
Tb.N	0.936**	-0.637**	0.608**	1	-0.984**	0.972**
Tb.Sp	-0.966**	0.735**	-0.709**	-0.984**	1	-0.930**
Conn.Dn	0.858**	-0.510**	0.472*	0.972**	-0.930**	1

* $p \leq 0.05$; ** $p < 0.01$; *** $p < 0.001$

Bone volume fraction was significantly correlated with the bone surface to volume ratio ($r=-0.862$, $p<0.001$), trabecular thickness ($r=0.845$, $p<0.001$), trabecular number

($r=0.936$, $p<0.001$), trabecular separation ($r=-0.966$, $p<0.001$) and connectivity density ($r=0.858$, $p<0.001$). Bone surface to volume ratio was significantly correlated with the trabecular thickness ($r=-0.996$, $p<0.001$), trabecular number ($r=-0.637$, $p=0.004$), trabecular separation ($r=-0.735$, $p=0.001$) and connectivity density ($r=-0.510$, $p=0.031$). Trabecular thickness was significantly correlated with the trabecular number ($r=0.608$, $p=0.007$), trabecular separation ($r=-0.709$, $p=0.001$) and connectivity density ($r=0.472$, $p=0.048$). Trabecular number was significantly correlated with the trabecular separation ($r=-0.984$, $p<0.001$) and connectivity density ($r=0.972$, $p<0.001$). Trabecular separation was significantly correlated with the connectivity density ($r=-0.930$, $p<0.001$).

Table 5.6 Pearson correlation coefficients between DXA, stochastic and microarchitecture parameters

	BMC	Sill	Nugget	BV/TV	BS/BV	Tb.Th	Tb.Sp
Area	0.746**	-0.280	-0.240	-0.532*	0.548*	-0.556*	0.478*
Range	-0.081	-0.062	0.873**	0.044	0.043	-0.005	-0.067
BMD	0.490*	0.820**	0.307	0.325	-0.203	0.233	-0.333

* $p \leq 0.05$; ** $p < 0.01$; *** $p < 0.001$

Area of vertebrae assessed by DXA was significantly correlated with the bone mineral content of vertebrae assessed by DXA ($r=0.746$, $p<0.001$), bone volume fraction ($r=-0.532$, $p=0.023$), bone surface to volume ratio ($r=0.548$, $p=0.019$), trabecular thickness ($r=-0.556$, $p=0.017$) and trabecular separation ($r=0.478$, $p=0.045$). Bone mineral content of vertebrae was correlated with the bone mineral density of vertebrae ($r=0.490$, $p=0.039$). Sill variance was significantly correlated with the bone mineral density ($r=0.820$, $p<0.001$). Range or correlation length was significantly correlated with nugget variance ($r=0.873$, $p<0.001$). BMD of vertebrae calculated from BMD map (Figure 4.3) was significantly correlated with BMD of vertebrae assessed by DXA ($r=0.946$, $p<0.001$).

5.4 Linear regression analysis of DXA, stochastic and microarchitecture parameters

Equation of best fit line with slope and y-intercept as well as coefficient of determination (R^2) were obtained for each linear regression analysis and specified in each Figure. Results of linear regression analysis of DXA, stochastic and microarchitecture parameters were provided below.

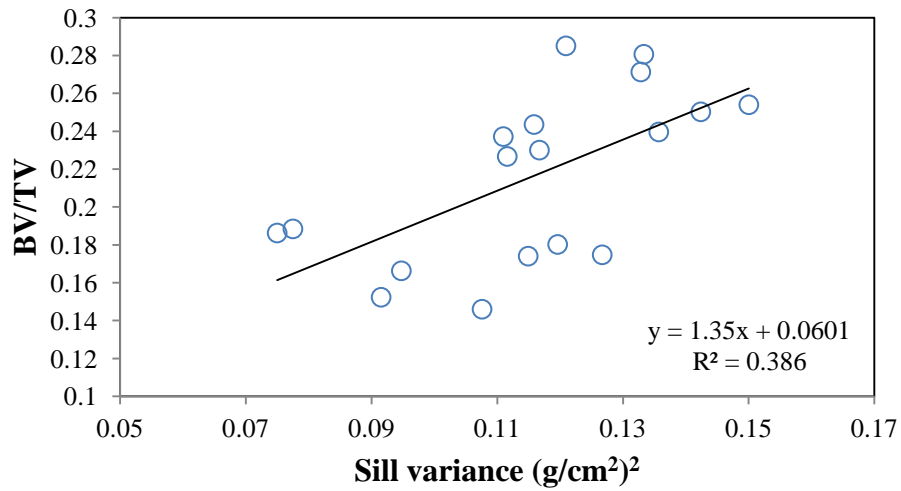


Figure 5.1 Linear regression analysis of sill variance and bone volume fraction

In the above linear regression analysis (Figure 5.1), sill variance was positively correlated with the bone volume fraction with coefficient of determination ($R^2=0.39$), slope of line ($m=1.35$) and y-intercept ($c=0.06$).

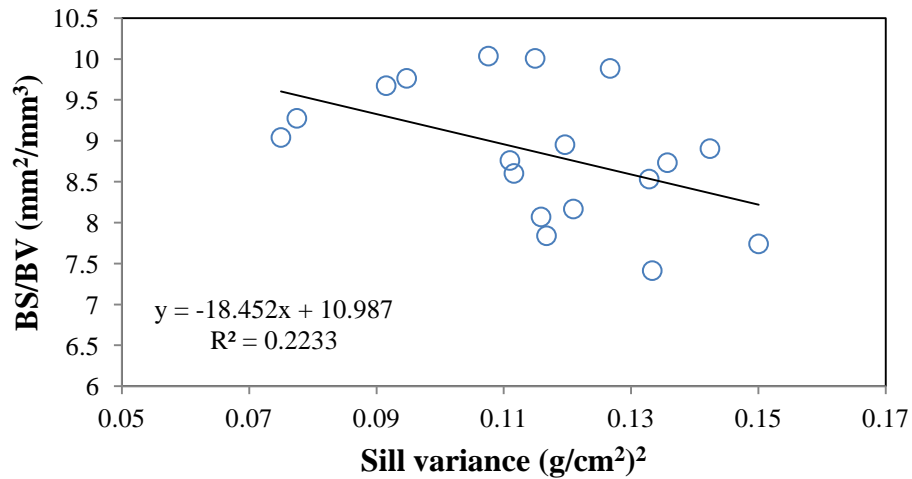


Figure 5.2 Linear regression analysis of sill variance and bone surface to volume ratio

In the above linear regression analysis (Figure 5.2), sill variance was negatively correlated with the bone surface to volume ratio ($R^2=0.22$, $m= -18.45$, $c=10.98$).

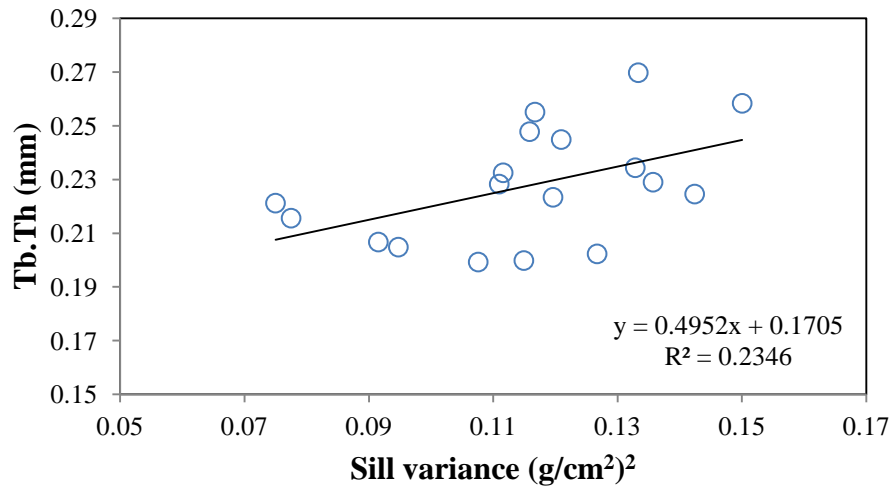


Figure 5.3 Linear regression analysis of sill variance and trabecular thickness

In the above analysis (Figure 5.3), sill variance of a BMD map was positively correlated with trabecular thickness ($R^2 = 0.23$) with slope of line ($m=0.49$) and y-intercept ($c=0.17$).

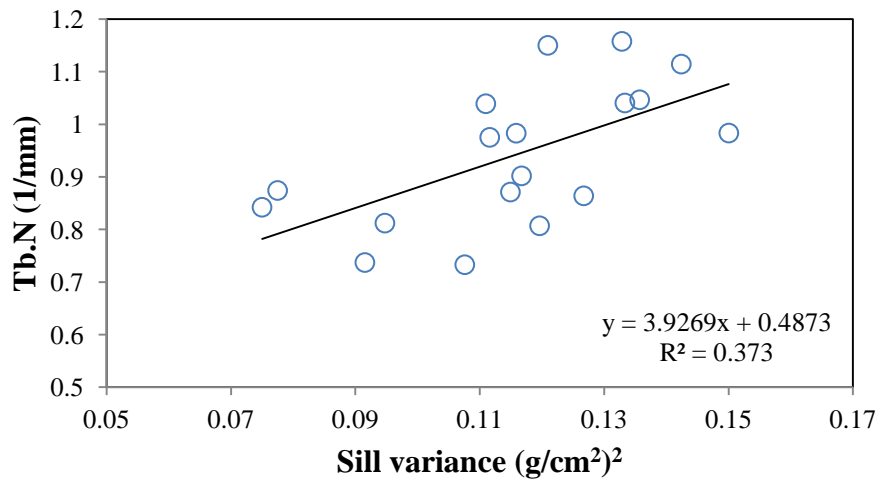


Figure 5.4 Linear regression analysis of sill variance and trabecular number

In the above analysis (Figure 5.4), sill variance of a BMD map was positively correlated with trabecular number ($R^2 = 0.37$) with slope of line ($m=3.92$) and y-intercept ($c=0.48$).

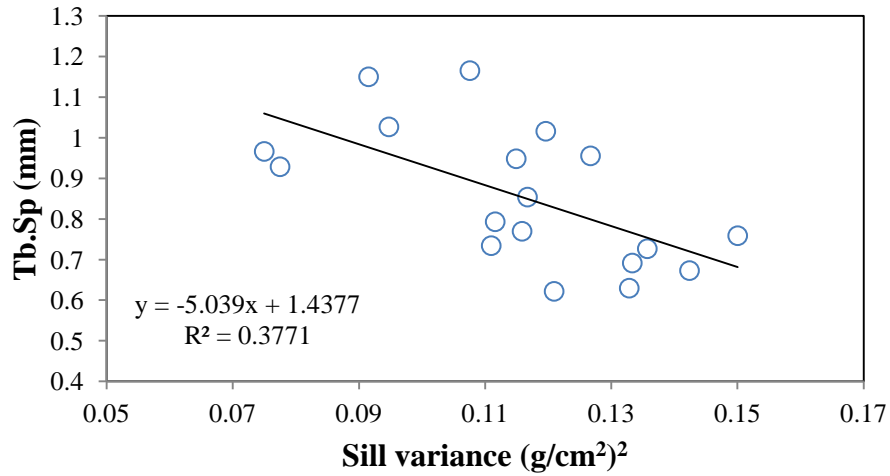


Figure 5.5 Linear regression analysis of sill variance and trabecular separation

In the above analysis (Figure 5.5), sill variance of a BMD map was negatively correlated with trabecular separation ($R^2=0.38$) with slope of line ($m=-5.039$) and y-intercept ($c=1.43$).

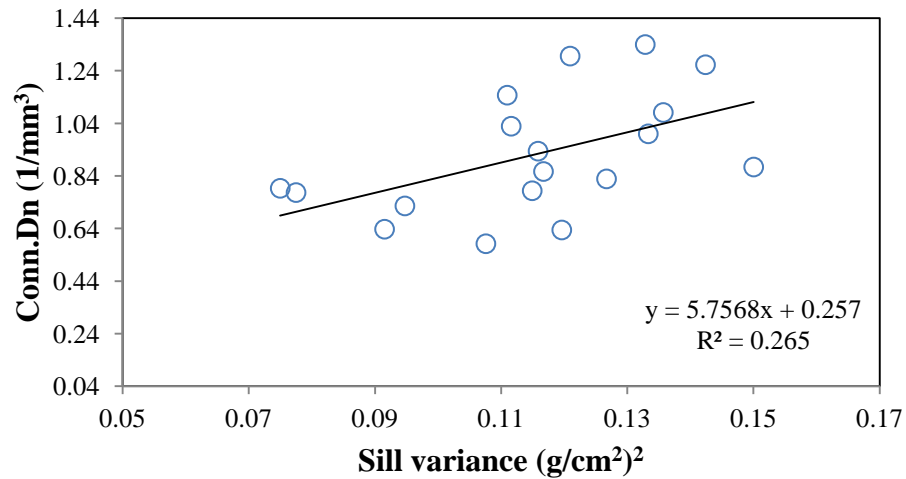


Figure 5.6 Linear regression analysis of sill variance and connectivity density

In the above analysis (Figure 5.6), sill variance of a BMD map was positively correlated with the connectivity density ($R^2=0.27$, $m=5.75$, $c=0.25$).

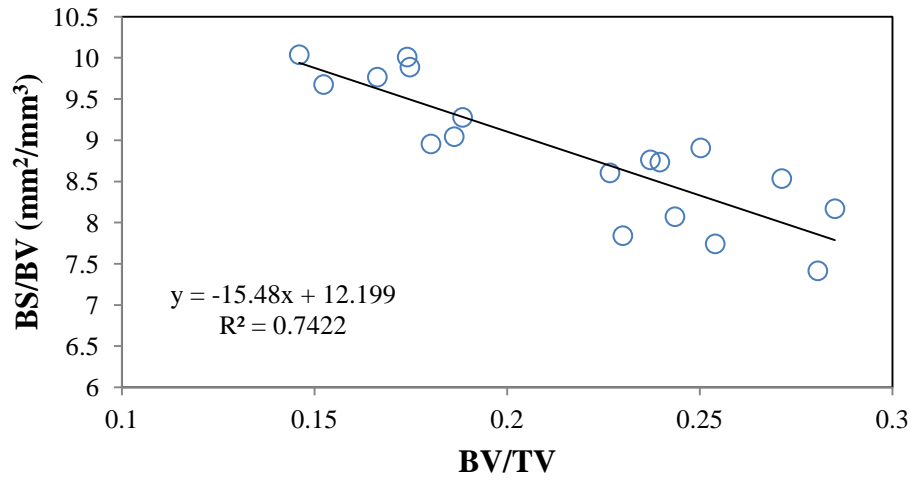


Figure 5.7 Linear regression analysis of bone volume fraction and surface to volume ratio

In the above linear regression analysis (Figure 5.7), bone volume fraction was negatively correlated with bone surface to volume ratio ($R^2=0.74$, $m=-15.48$, $c=12.19$).

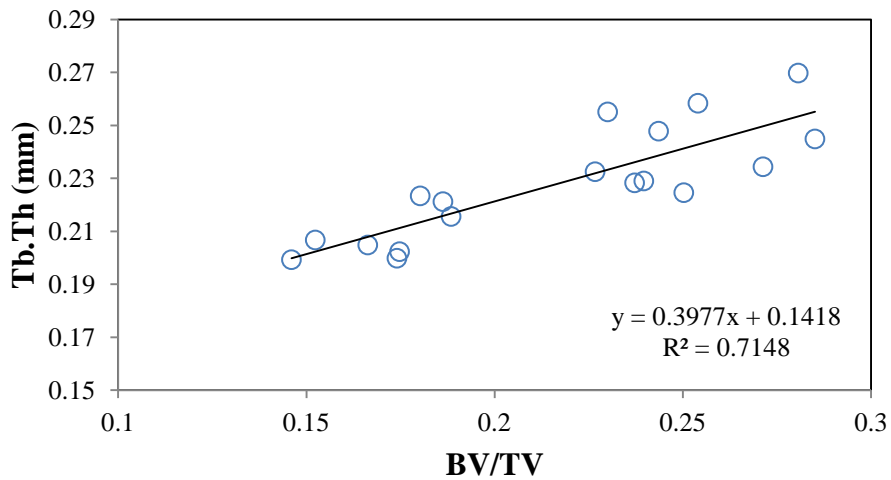


Figure 5.8 Linear regression analysis of bone volume fraction and trabecular thickness

In the above linear regression analysis (Figure 5.8), bone volume fraction was significantly positively correlated with trabecular thickness ($R^2=0.72$, $m= 0.397$, $c=0.142$).

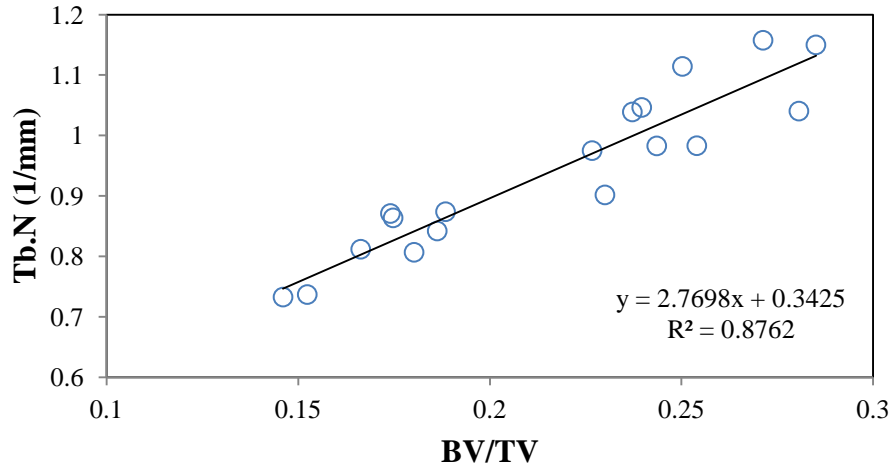


Figure 5.9 Linear regression analysis of bone volume fraction and trabecular number

In the above linear regression analysis (Figure 5.9), bone volume fraction was significantly positively correlated with trabecular number ($R^2=0.88$, $m=2.76$, $c=0.342$).

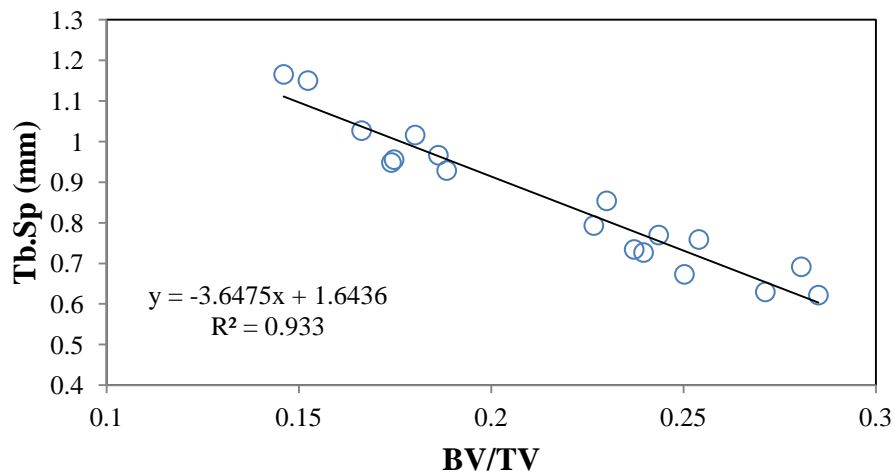


Figure 5.10 Linear regression analysis of bone volume fraction and trabecular separation

In the above linear regression analysis (Figure 5.10), bone volume fraction was significantly negatively correlated with trabecular separation ($R^2=0.93$, $m=-3.647$, $c=1.643$).

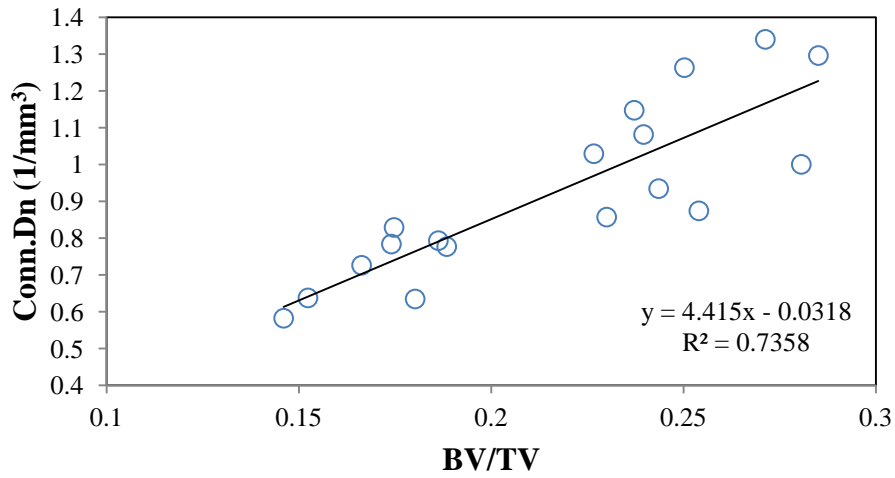


Figure 5.11 Linear regression analysis of bone volume fraction and connectivity density

In the above linear regression analysis (Figure 5.11), bone volume fraction was significantly positively correlated with connectivity density ($R^2=0.74$, $m=4.415$, $c=-0.032$).

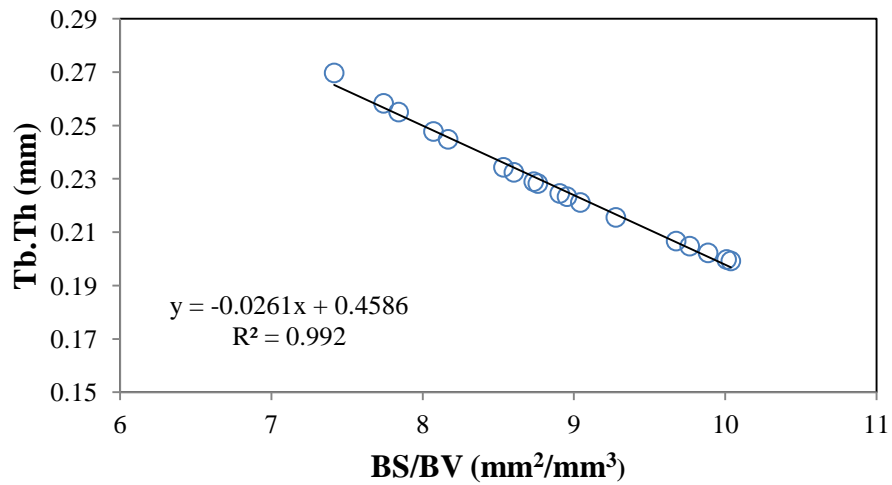


Figure 5.12 Linear regression analysis of surface to volume ratio and trabecular thickness

In the above analysis (Figure 5.12), bone surface to volume ratio was significantly negatively correlated with trabecular thickness ($R^2=0.99$, $m=-0.0261$, $c=-0.458$).

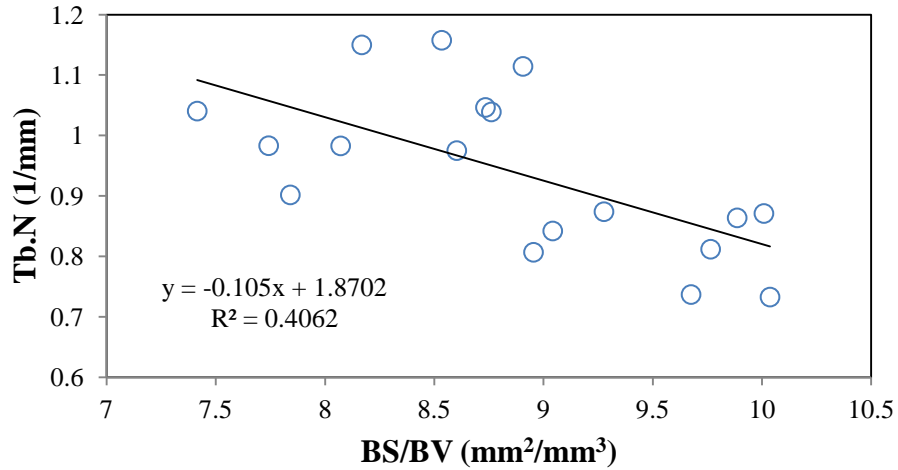


Figure 5.13 Linear regression analysis of surface to volume ratio and trabecular number

In the above linear regression analysis (Figure 5.13), bone surface to volume ratio was negatively correlated with trabecular number ($R^2=0.41$, $m=-0.105$, $c=1.87$).

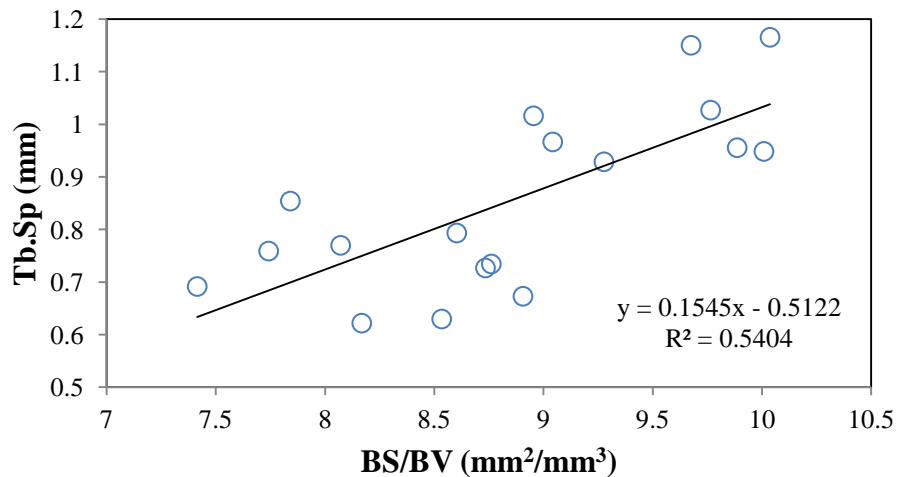


Figure 5.14 Linear regression analysis of bone surface to volume ratio and trabecular separation

In the above linear regression analysis (Figure 5.14), bone surface to volume ratio was positively correlated with trabecular separation ($R^2=0.54$, $m=0.154$, $c=-0.512$).

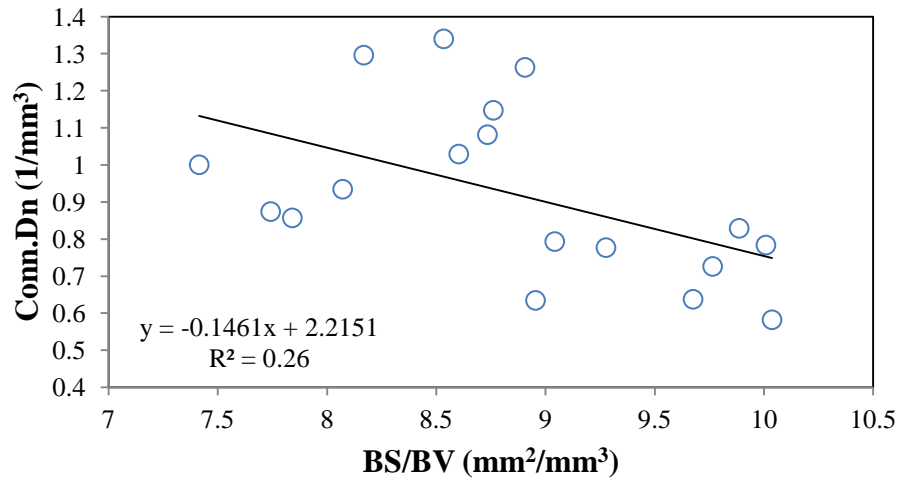


Figure 5.15 Linear regression analysis of surface to volume ratio and connectivity density

In the above linear regression analysis (Figure 5.15), bone surface to volume ratio was negatively correlated with connectivity density ($R^2=0.26$, $m=-0.146$, $c=2.215$).

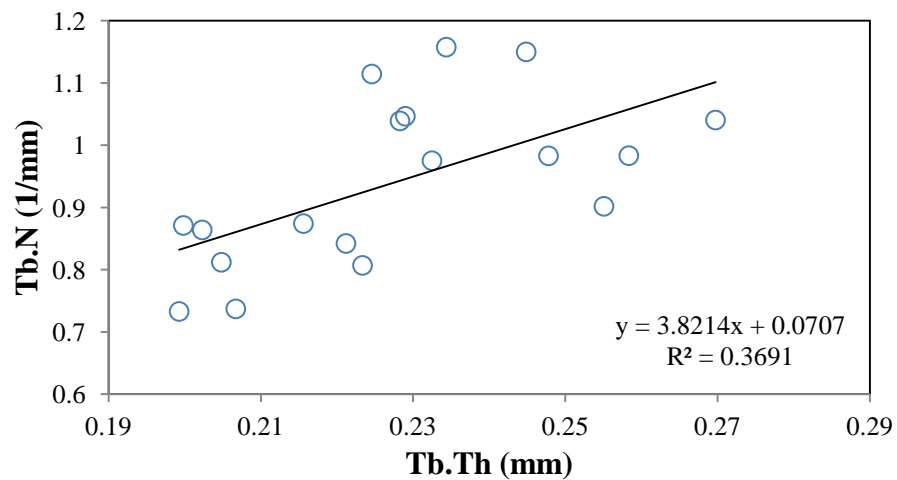


Figure 5.16 Linear regression analysis of trabecular thickness and trabecular number

In the above linear regression analysis (Figure 5.16), trabecular thickness and trabecular number were positively correlated ($R^2=0.36$, $m=3.821$, $c=0.07$).

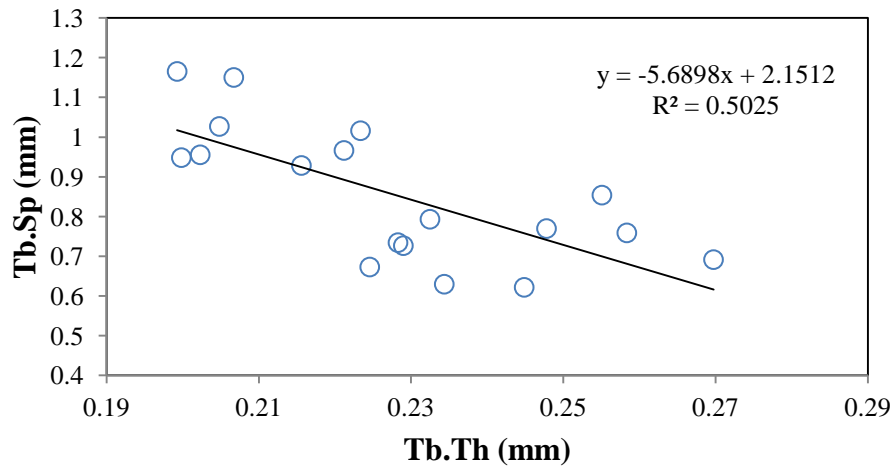


Figure 5.17 Linear regression analysis of trabecular thickness and trabecular separation

In the above linear regression analysis (Figure 5.17), trabecular thickness and trabecular separation were significantly negatively correlated ($R^2=0.50$, $m=-5.69$, $c=0.50$).

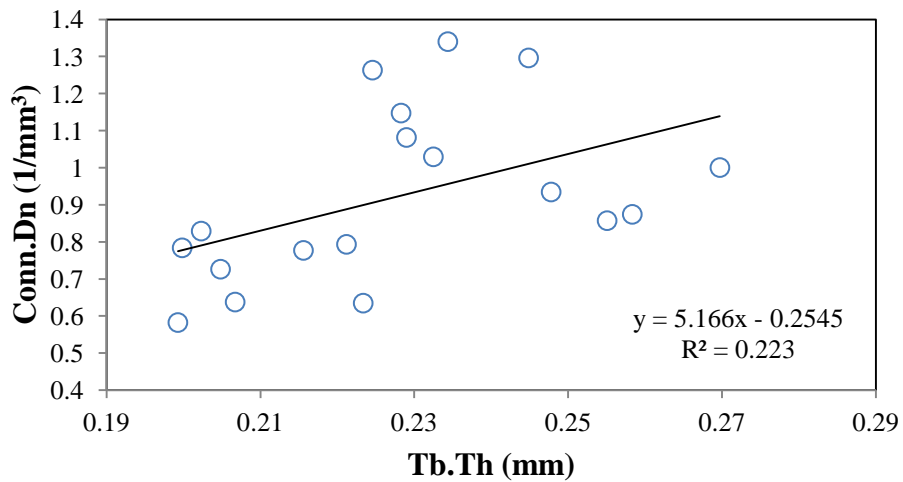


Figure 5.18 Linear regression analysis of trabecular thickness and connectivity density

In the above linear regression analysis (Figure 5.18), trabecular thickness and connectivity density were positively correlated ($R^2=0.22$, $m=5.16$, $c=-0.25$).

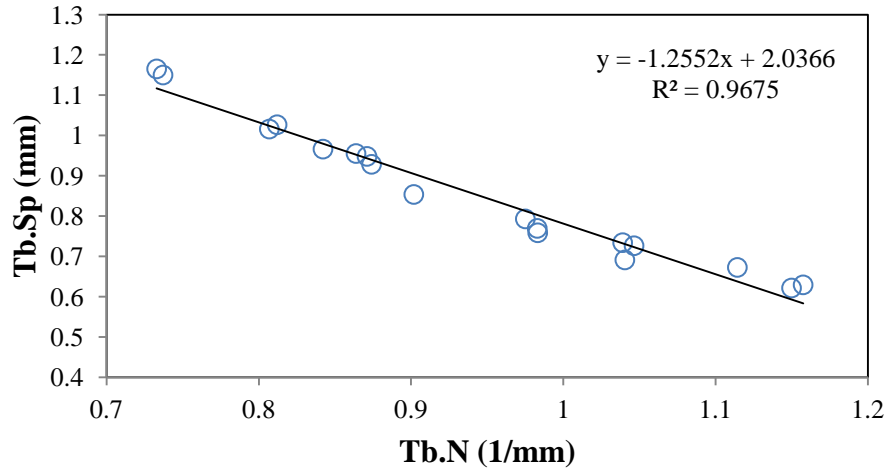


Figure 5.19 Linear regression analysis of trabecular number and trabecular separation

In the above linear regression analysis (Figure 5.19), trabecular number and trabecular separation were significantly negatively correlated ($R^2=0.97$, $m=-1.25$, $c=2.03$).

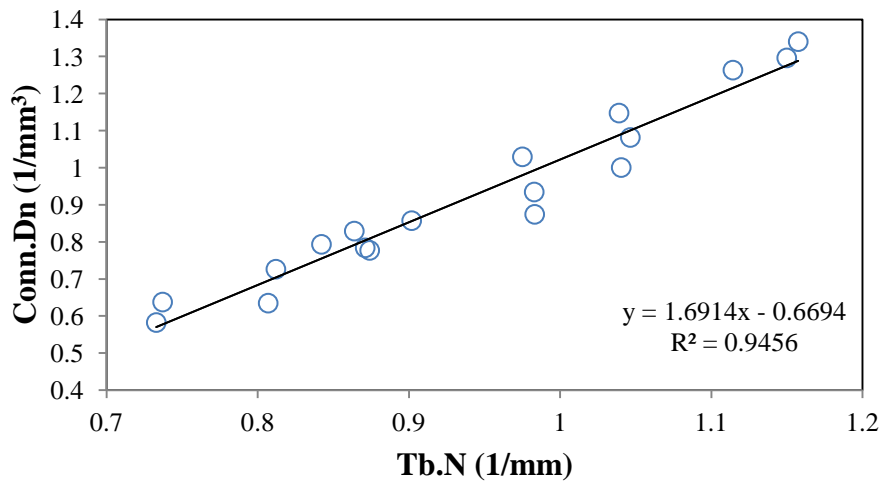


Figure 5.20 Linear regression analysis of trabecular number and connectivity density

In the above linear regression analysis (Figure 5.20), trabecular number and connectivity density were significantly positively correlated ($R^2=0.95$, $m=1.69$, $c=-0.669$).

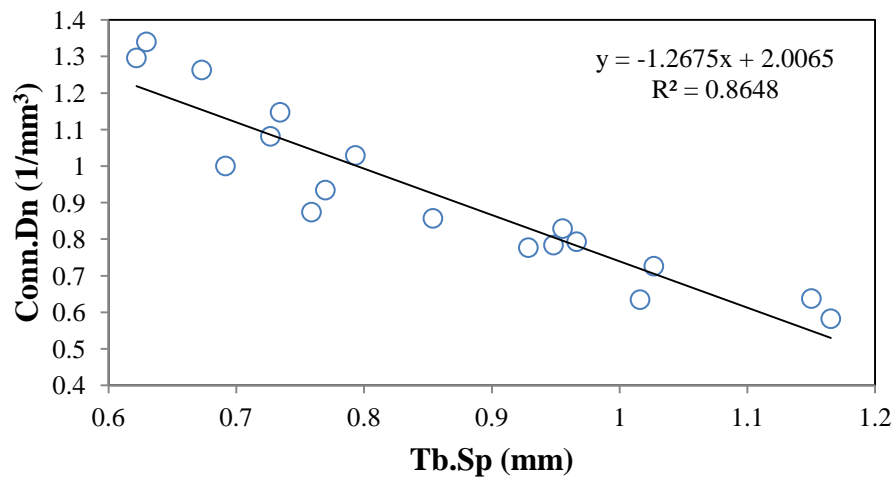


Figure 5.21 Linear regression analysis of trabecular separation and connectivity density

In the above linear regression analysis (Figure 5.21), trabecular separation and connectivity density were negatively correlated ($R^2=0.86$, $m=-1.267$, $c=2.006$).

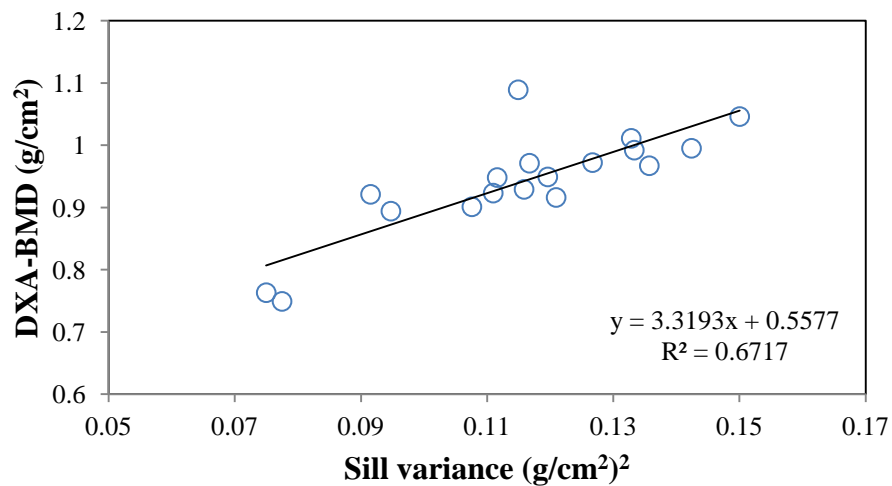


Figure 5.22 Linear regression analysis of sill variance and bone mineral density

In the above linear regression analysis (Figure 5.22), sill variance was significantly positively correlated with bone mineral density assessed by DXA ($R^2=0.67$, $m=3.13$, $c=0.55$).

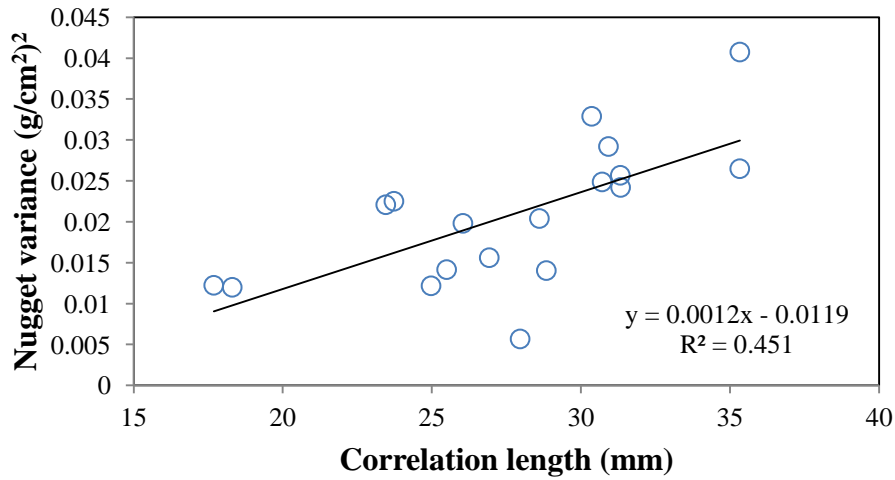


Figure 5.23 Linear regression analysis of correlation length and nugget variance

In the above linear regression analysis (Figure 5.23), correlation length was positively correlated with nugget variance ($R^2 = 0.45$, $m = 0.001$, $c = -0.012$).

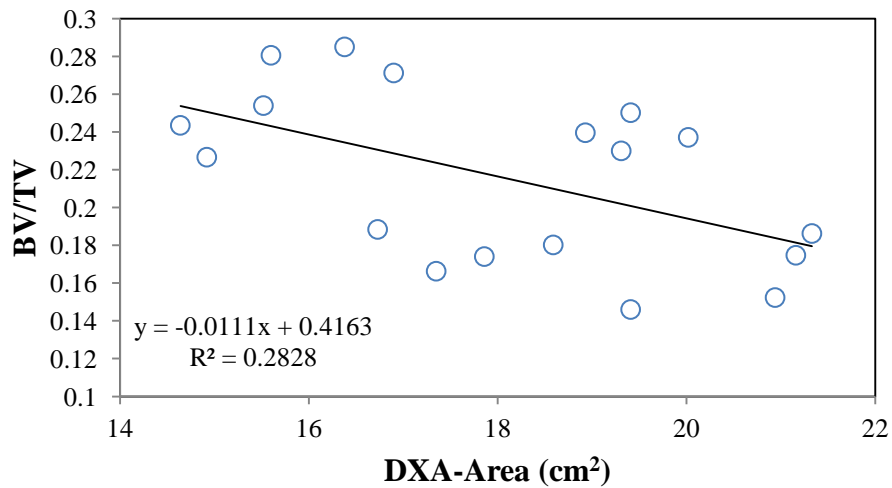


Figure 5.24 Linear regression analysis of area of specimen and bone volume fraction

In the above linear regression analysis (Figure 5.24), area of vertebrae assessed by DXA was negatively correlated with bone volume fraction ($R^2 = 0.28$, $m = -0.011$, $c = 0.416$).

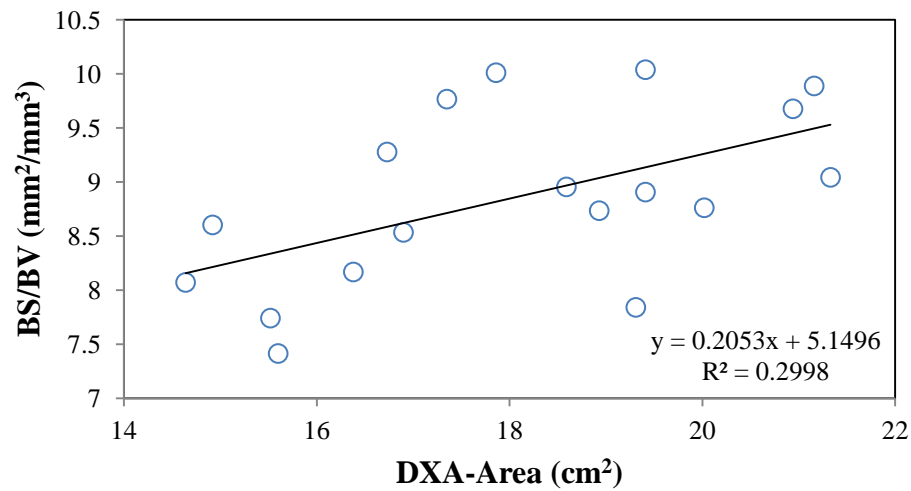


Figure 5.25 Linear regression analysis of area of specimen and surface to volume ratio

In the above linear regression analysis (Figure 5.25), area of vertebrae assessed by DXA was positively correlated with bone surface to volume ratio ($R^2 = 0.30$, $m = 0.205$, $c = 5.14$).

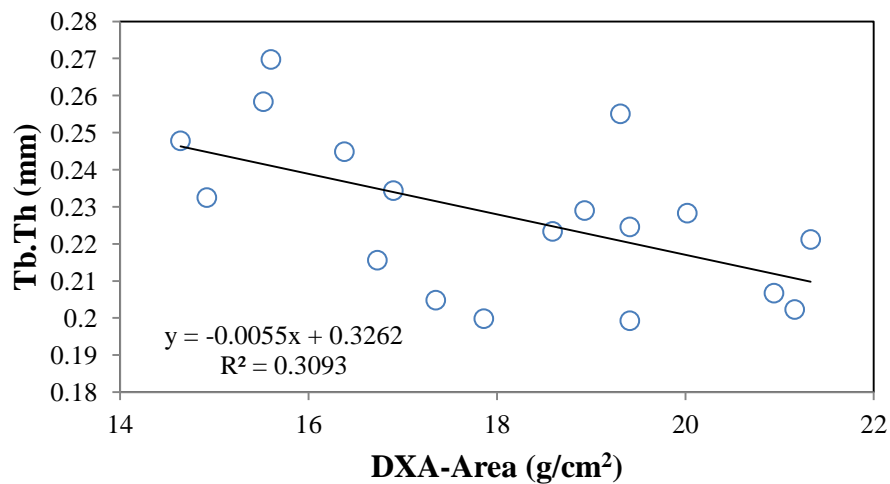


Figure 5.26 Linear regression analysis of area of specimen and trabecular thickness

In the above linear regression analysis (Figure 5.26), area of vertebrae assessed by DXA was negatively correlated with trabecular thickness ($R^2 = 0.31$, $m = -0.005$, $c = 0.326$).

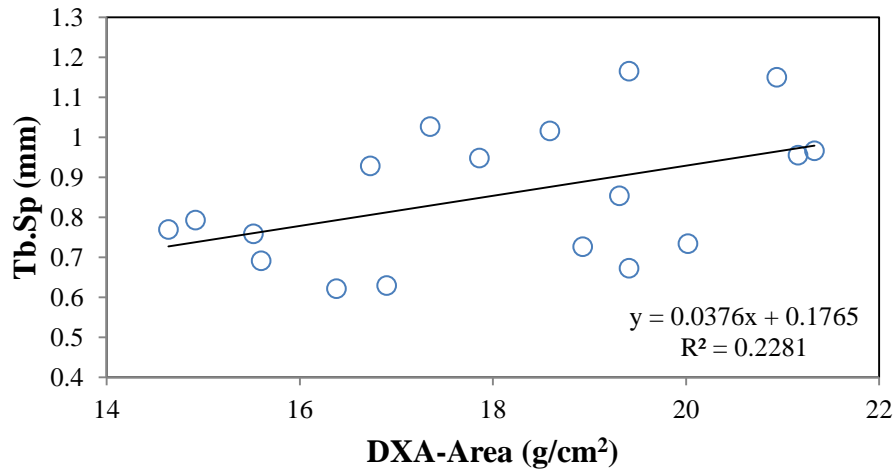


Figure 5.27 Linear regression analysis of area of specimen and trabecular separation

In the above linear regression analysis (Figure 5.27), area of vertebrae assessed by DXA was positively correlated with trabecular separation ($R^2=0.23$, $m=0.0376$, $c=0.176$).

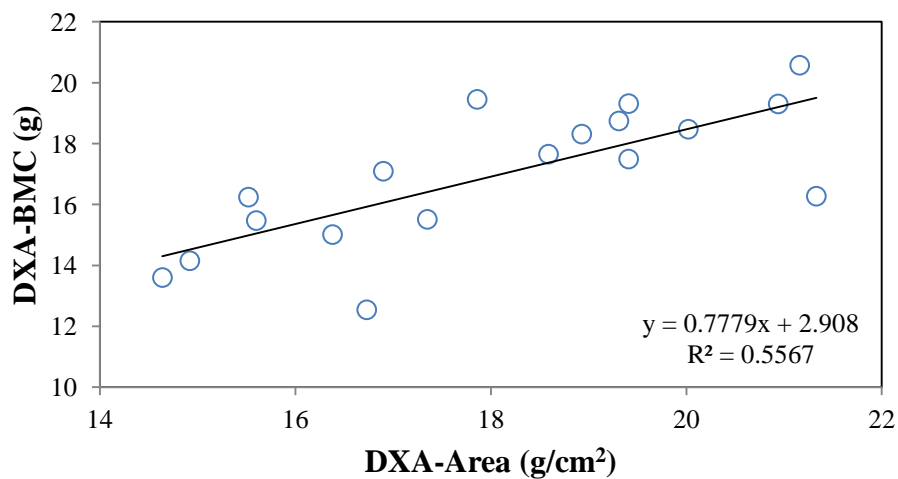


Figure 5.28 Linear regression analysis of area and bone mineral content of the vertebrae

In the above linear regression analysis (Figure 5.28), area of vertebrae assessed by DXA was significantly positively correlated with bone mineral content of vertebrae assessed by DXA ($R^2=0.56$, $m=0.778$, $c=2.908$).

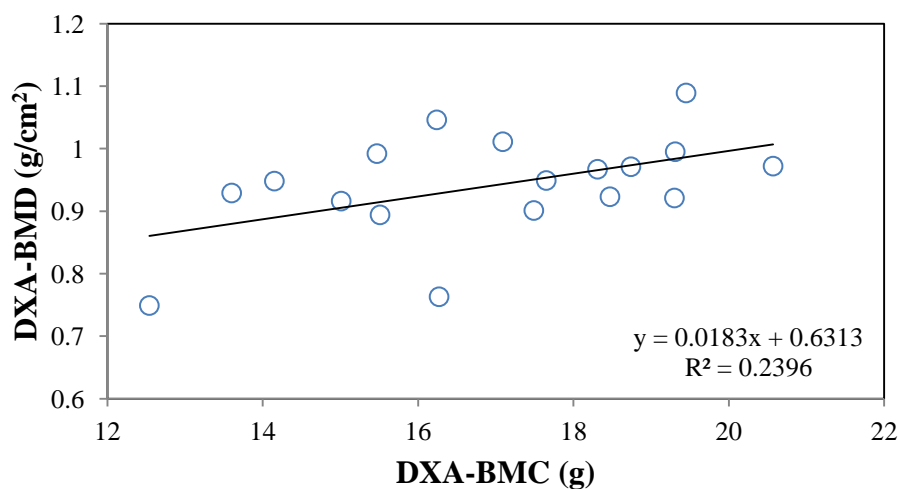


Figure 5.29 Linear regression analysis of bone mineral content and bone mineral density

In the above analysis (Figure 5.29), bone mineral content of vertebrae was positively correlated with bone mineral density of vertebrae ($R^2 = 0.24$, $m = 0.018$, $c = 0.63$).

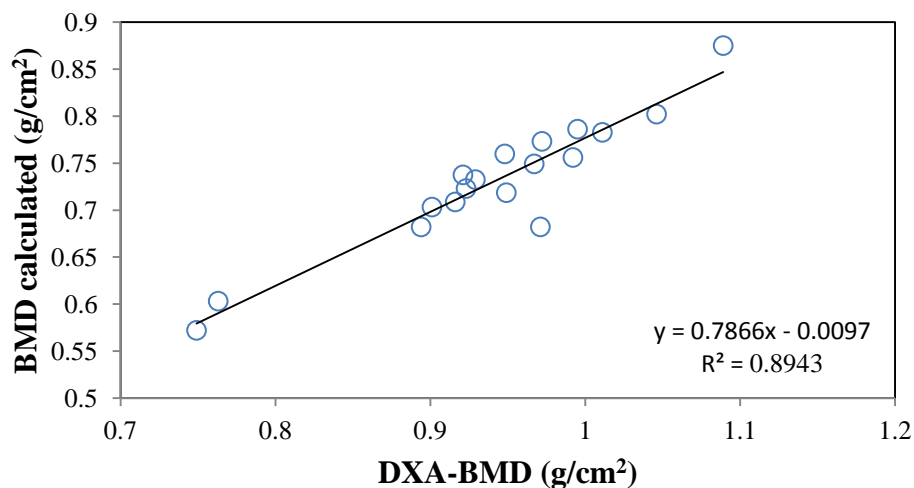


Figure 5.30 Linear regression analysis of DXA-BMD and BMD calculated

In the above linear regression analysis (Figure 5.30), BMD assessed by DXA and BMD calculated from the raw data files of DXA were strongly correlated ($R^2 = 0.89$, $m = 0.786$, $c = -0.009$).

CHAPTER SIX

DISCUSSION AND CONCLUSION

In this study, eighteen human vertebrae with intact posterior elements were scanned by the DXA scanner in the posterior-anterior projection and by the Micro-CT scanner. The stochastic predictors were calculated from the BMD map of human vertebrae from DXA scans. The microarchitecture parameters were obtained from 3D Micro-CT images of trabecular bone within the vertebral body. Significant correlations were observed between stochastic predictors and microarchitecture parameters of trabecular bone. The sill variance, one of stochastic predictors from DXA scans, was significantly correlated with the microarchitecture parameters of trabecular bone. These correlations were consistent with the observations reported in the literature [15, 16, 19, 27].

6.1 DXA measurements of human lumbar vertebrae

DXA measurements (BMD, BMC and area) of human lumbar vertebrae (L1-L5) in the PA projection were in agreement with results reported in literature [19, 38, 39]. Submersion of human vertebrae under water simulates the *in-vivo* environment with soft tissue. The unique shapes of the posterior elements of the lumbar vertebrae were observed. The posterior elements of L1, L2 and L3 had a U-shaped or Y-shaped appearance. The posterior elements of L4 had a H or X shaped appearance and the posterior elements of L5 looked like a block I on its side. The significant increase in BMC and area from L1 to L4 and the significant increase in BMD between L1 and L2 was consistent with the data reported in a study of 148 normal women aged 50-60 [39]. The contribution of posterior elements to the calcium hydroxyapatite content of whole vertebrae measured in the PA projection was as high as 47.0 % [40]. Therefore, current BMD measurements ($0.941 \pm 0.084 \text{ g/cm}^2$) were higher than the BMD measurements ($0.567 \pm 0.09 \text{ g/cm}^2$) of the *in-vitro* DXA scans of human vertebrae without posterior elements [19, 41].

6.2 Microarchitecture parameters within the vertebral body

Microarchitecture parameters of trabecular bone within the vertebral body obtained in this study were in agreement with the data reported in earlier studies [15, 19, 26, 27]. The bone volume fraction (0.215 ± 0.045 , range from 0.146 to 0.285) of this study was comparable to results from a study using Micro-CT scanners with a voxel size of $119 \mu\text{m}$ [42] and a voxel size of $93 \mu\text{m}$ [16]. However, bone volume fraction from this study was greater than the measurement from the studies with higher scanning resolutions. For example, the bone volume fraction (0.215 ± 0.045) of this study was greater than those (0.062 ± 0.017) from Micro-CT scans with a resolution of $17.4 \mu\text{m}$ [43] and those in another study (0.153 ± 0.051) with a scanning resolution of $35 \mu\text{m}$ [44]. Trabecular thickness measurements in this study ($0.227 \pm 0.021 \text{ mm}$) were in agreement with the previous study of ($0.224 \pm 0.044 \text{ mm}$) [44] and ($0.228 \pm 0.046 \text{ mm}$) [16]. Bone volume fraction was significantly positively correlated with trabecular thickness, trabecular number, connectivity density and negatively correlated with bone surface to volume ratio, trabecular separation. The correlations between bone volume fraction and remaining microarchitecture parameters were consistent with the results in earlier studies [15, 27].

6.3 Correlations between stochastic predictors and microarchitecture parameters

Significant relationships between the sill variance of DXA scans and microarchitecture parameters were consistent with the previous study of 2D projections images [27] and other studies based on the experimental variogram [15, 16, 19]. In the previous study of 2D projection images generated from 3D Micro-CT images of trabecular bone, we have also observed that the sill variance was positively correlated with bone volume fraction, trabecular thickness, and trabecular number, but negatively correlated with bone surface to volume ratio and bone separation [27]. Positive relationship between sill variance and trabecular thickness and the negative relationship between sill variance and trabecular separations indicated that decreases in bone heterogeneity led to the increases in bone fragility [45].

It may not be surprising that significant relationships are observed between stochastic predictors of DXA scans and microarchitecture parameters of trabecular bone because both stochastic assessment and microarchitecture quantification share the same

underlying principles. Microarchitecture parameters of trabecular bone, such as bone volume fraction, bone surface to volume fraction, and connectivity density, are evaluated by traditional histomorphometry [46], which is based on stereological techniques [47]. The underlying principles of stereological techniques come from stochastic geometry [48]. In this study, the random field, a major part of stochastic geometry, is also the theoretical basis for the stochastic assessment of the BMD map from DXA scans [27, 49]. Therefore, it is expected that there are certain connections between stochastic assessment and microarchitecture quantification. Nevertheless, such connections need to be further studied in the future.

The sill variance from DXA scans, to some extent, represents the standard deviation of bone mineral density within human vertebrae, and characterizes the inhomogeneity of bone mineral density within human vertebrae. Such variation of bone mineral density has been found to be a good predictor of biomechanical properties of the human vertebral body [50]. In the previous study, Cody *et al.* indicated the surprise that the standard deviation of vertebral regional bone mineral density values provided nearly as good as a predictor of fracture load as the densities themselves [50]. The authors have concluded that local remodeling effects, causing point-to-point variations of bone mineral density in specific locations, may ultimately be helpful in predicting fracture risk in conjunction with local bone density analysis [50]. Therefore, the sill variance observed in this study may reveal the point-to-point variations of bone mineral density due to local bone remodeling.

6.4 Comparison of stochastic assessment with existing imaging techniques

Stochastic assessment can be distinguished from other imaging techniques to enhance the prediction of bone fractures from 2D projection images in the following aspects.

Fractal texture analysis is a popular image processing technique which can be used to extract hidden geometric and microarchitecture features of bone from high resolution 2D radiography images. Texture parameters evaluated from X-ray radiographs of iliac bone, osteoporotic femurs, femoral head are significantly correlated with microarchitecture parameters of bone in earlier studies [23-25]. Although the texture parameters showed significant relationships with microarchitecture parameters, texture analysis has rarely

been applied to 2D projection images of DXA scans where as the stochastic assessment can be successfully apply to the routine clinical DXA scans.

Topological parameter based on Minkowski function can be evaluated using topological analysis that has been applied to 2D-DXA images. An *in-vitro* study of 100 hip specimens demonstrated that the topology-based parameter from DXA images had a strong correlation with the failure strength of the specimens [51].

Both hip structural analysis and finite element analysis of X-ray images are the popular techniques implemented by researchers to extract stiffness and strength of the bone from DXA scans. The use of hip structural analysis is limited by the precision error of femur positioning by the technologist during DXA scans [52, 53]. The stiffness of the proximal femur can be numerically estimated from the finite element analysis, which has shown significant correlations with the stiffness measured from mechanical testing. This approach has only been validated in an *ex-vivo* study and its application to routine clinical DXA images remains to be established in the future [13].

In recent years, the Trabecular Bone Score (TBS) has gained the attention of researchers in the assessment of fracture risk [54, 55]. TBS is based on the variation of the grayscale values of DXA images, rather than a property with direct physical meaning [15, 17]. Stochastic predictors are based on the variation of bone mineral density values from the BMD map of DXA scans. The value of bone mineral density at each location was obtained from the raw data of DXA scans (i.e., R files in Hologic densitometers) using the equations of mass attenuation for dual-energy X-ray absorptiometry [34, 35]. The use of BMD maps may facilitate the comparison of results when multicenter studies are conducted to predict osteoporotic fractures.

TBS describes only one aspect of experimental variograms whereas the stochastic predictors we proposed represent a comprehensive view of experimental variograms. TBS is calculated as the slope at the origin of the log-log representation of experimental variograms [15-18]. The initial trend of the experimental variogram may be described by the TBS. However, the final trend in the experiment variogram is not represented by the

TBS. On the other hand, stochastic predictors are derived from a theoretical model of random fields that captures the global trend of the experimental variogram.

Stochastic assessments of bone mineral distribution from DXA scans may supplement the clinical use of FRAX in predicting the risk of osteoporotic fractures. FRAX is a fracture risk assessment tool that uses clinical risk factors with or without BMD to predict the absolute 10-year probability of hip fracture or major osteoporotic fracture in general [56]. The prediction of fracture risk through FRAX is useful in clinical practice. However, there are several limitations for FRAX in clinical practice. First, questions may not be answered accurately by patients. For example, one of questions is whether the patient has a history of rheumatoid arthritis. Sometimes patients with osteoarthritis may indicate that they have rheumatoid arthritis because they just don't know the difference between rheumatoid arthritis and osteoarthritis [38]. Additionally, FRAX is not applicable to patients who have drug therapy for bone [56].

6.5 Limitations and future work

This study has several limitations that can be addressed in future work. First, the number of subjects (cadavers spines) used in this study is small, even though the total number of vertebral specimens are eighteen. Second, only Hologic QDR Discovery W is used in this study, we can extend our study to other manufacturers of densitometers. Third, low resolution (92 μm) micro-CT images of specimens are used. This suggests that accuracy of measuring microarchitecture parameters of trabecular bone can be improved using high resolution (20 μm) micro-CT images. Fourth, currently this study establishes the relationship between stochastic parameters and microarchitecture parameters only. In the future, biomechanical properties (elastic modulus and ultimate strength) of trabecular bone in lumbar vertebrae can be measured to determine the relationship between stochastic parameters and biomechanical properties of bone. Finally, stochastic parameters are currently evaluated on DXA scans of human vertebrae in the posterior anterior (PA) projection. This method can be applied to the DXA scans of specimens in the lateral projection.

6.6 Conclusion

This study has described the stochastic assessment of bone mineral density variation in human vertebrae and demonstrated the relationship between stochastic assessment and bone microarchitecture. Sill variance, a stochastic measure of vertebrae BMD map establishes strong correlations with microarchitecture parameters of vertebral body. This study demonstrates that the stochastic assessment of the inhomogeneity of bone mineral density from routine clinical DXA scans of human lumbar vertebrae may have the potential to serve as a valuable clinical tool in enhancing the prediction of risks for osteoporotic fractures in the spine. The main advantage of using DXA scans is that it would be cost effective, since most hospitals already have DXA machines and there would be no need for purchasing new equipment. Therefore, the stochastic method can provide an effective and economic solution for the prediction of osteoporotic fractures in the lumbar spine.

REFERENCES

- [1] "NIH Consensus Development Panel on Osteoporosis Prevention, Diagnosis, and Therapy, March 7-29, 2000: highlights of the conference," *South Med J*, vol. 94, pp. 569-73, Jun 2001.
- [2] M. L. Bouxsein, "Bone quality: where do we go from here?," *Osteoporos Int*, vol. 14 Suppl 5, pp. S118-27, Sep 2003.
- [3] L. Apostol, *et al.*, "Relevance of 2D radiographic texture analysis for the assessment of 3D bone micro-architecture," *Med Phys*, vol. 33, pp. 3546-56, Sep 2006.
- [4] C. L. Benhamou, *et al.*, "Fractal organization of trabecular bone images on calcaneus radiographs," *J Bone Miner Res*, vol. 9, pp. 1909-18, Dec 1994.
- [5] J. C. Buckland-Wright, *et al.*, "Fractal signature analysis of macroradiographs measures trabecular organization in lumbar vertebrae of postmenopausal women," *Calcif Tissue Int* vol. 54, pp. 106-12, 1994.
- [6] D. Chappard, *et al.*, "Texture analysis of X-ray radiographs is a more reliable descriptor of bone loss than mineral content in a rat model of localized disuse induced by the Clostridium botulinum toxin," *Bone*, vol. 28, pp. 72-9, Jan 2001.
- [7] T. Le Corroller, *et al.*, "Combination of texture analysis and bone mineral density improves the prediction of fracture load in human femurs," *Osteoporos Int*, vol. 23, pp. 163-9, Jan 2012.
- [8] E. Lespessailles, *et al.*, "Clinical interest of bone texture analysis in osteoporosis: a case control multicenter study," *Osteoporos Int*, vol. 19, pp. 1019-28, Jul 2008.
- [9] S. Majumdar, *et al.*, "Application of fractal geometry techniques to the study of trabecular bone," *Med Phys*, vol. 20, pp. 1611-9, Nov-Dec 1993.
- [10] S. Majumdar, *et al.*, "In vivo assessment of trabecular bone structure using fractal analysis of distal radius radiographs," *Med Phys* vol. 27, pp. 2549-9, 2000.

- [11] E. A. Messent, *et al.*, "Fractal analysis of trabecular bone in knee osteoarthritis (OA) is a more sensitive marker of disease status than bone mineral density (BMD)," *Calcif Tissue Int*, vol. 76, pp. 419-25, Jun 2005.
- [12] L. Pothuaud, *et al.*, "Fractal dimension of trabecular bone projection texture is related to three-dimensional microarchitecture," *J Bone Miner Res*, vol. 15, pp. 691-9, Apr 2000.
- [13] C. M. Langton, *et al.*, "Comparison of 3D finite element analysis derived stiffness and BMD to determine the failure load of the excised proximal femur," *Med Eng Phys*, vol. 31, pp. 668-72, Jul 2009.
- [14] H. F. Boehm, *et al.*, "Differentiation between post-menopausal women with and without hip fractures: enhanced evaluation of clinical DXA by topological analysis of the mineral distribution in the scan images," *Osteoporos Int*, vol. 18, pp. 779-87, Jun 2007.
- [15] L. Pothuaud, *et al.*, "Correlations between grey-level variations in 2D projection images (TBS) and 3D microarchitecture: applications in the study of human trabecular bone microarchitecture," *Bone*, vol. 42, pp. 775-87, Apr 2008.
- [16] D. Hans, *et al.*, "Correlations between trabecular bone score, measured using anteroposterior dual-energy X-ray absorptiometry acquisition, and 3-dimensional parameters of bone microarchitecture: an experimental study on human cadaver vertebrae," *J Clin Densitom*, vol. 14, pp. 302-12, Jul-Sep 2011.
- [17] L. Pothuaud, *et al.*, "Evaluation of the potential use of trabecular bone score to complement bone mineral density in the diagnosis of osteoporosis: a preliminary spine BMD-matched, case-control study," *J Clin Densitom*, vol. 12, pp. 170-6, Apr-Jun 2009.
- [18] R. Winzenrieth, *et al.*, "Three-dimensional (3D) microarchitecture correlations with 2D projection image gray-level variations assessed by trabecular bone score using high-resolution computed tomographic acquisitions: effects of resolution and noise," *J Clin Densitom*, vol. 16, pp. 287-96, Jul-Sep 2013.
- [19] J. P. Roux, *et al.*, "The predictive value of trabecular bone score (TBS) on whole lumbar vertebrae mechanics: an ex vivo study," *Osteoporos Int*, vol. 24, pp. 2455-60, Sep 2013.

- [20] B. Rabier, *et al.*, "A multicentre, retrospective case-control study assessing the role of trabecular bone score (TBS) in menopausal Caucasian women with low areal bone mineral density (BMDa): Analysing the odds of vertebral fracture," *Bone*, vol. 46, pp. 176-81, Jan 2010.
- [21] R. Winzenrieth, *et al.*, "A retrospective case-control study assessing the role of trabecular bone score in postmenopausal Caucasian women with osteopenia: analyzing the odds of vertebral fracture," *Calcif Tissue Int*, vol. 86, pp. 104-9, Feb 2010.
- [22] J. N. Marija, *SPSS Statistics 17.0 Guide to Data Analysis*. NJ: Prentice Hall Inc., 2008.
- [23] P. Guggenbuhl, *et al.*, "Texture analysis of X-ray radiographs of iliac bone is correlated with bone micro-CT," *Osteoporos Int*, vol. 17, pp. 447-54, 2006.
- [24] T. Le Corroller, *et al.*, "Bone texture analysis is correlated with three-dimensional microarchitecture and mechanical properties of trabecular bone in osteoporotic femurs," *J Bone Miner Metab*, vol. 31, pp. 82-8, Jan 2013.
- [25] M. Ollivier, *et al.*, "Radiographic bone texture analysis is correlated with 3D microarchitecture in the femoral head, and improves the estimation of the femoral neck fracture risk when combined with bone mineral density," *Eur J Radiol*, vol. 82, pp. 1494-8, Sep 2013.
- [26] A. W. Popp, *et al.*, "Microstructural parameters of bone evaluated using HR-pQCT correlate with the DXA-derived cortical index and the trabecular bone score in a cohort of randomly selected premenopausal women," *PLoS One*, vol. 9, p. e88946, 2014.
- [27] X. N. Dong, *et al.*, "Biomechanical properties and microarchitecture parameters of trabecular bone are correlated with stochastic measures of 2D projection images," *Bone*, vol. 56, pp. 327-36, Oct 2013.
- [28] E. S. Orwell and S. K. Oviatt, "Longitudinal precision of dualenergy x-ray absorptiometry in a multicenter study," *J Bone Min Res* vol. 6, pp. 191-197, 1991.

- [29] T. Storm, *et al.*, "Effect of intermittent cyclical etidronate therapy on bone mass and fracture rate in women with postmenopausal osteoporosis," *N Engl J Med*, vol. 322, pp. 1265-71, May 3 1990.
- [30] G. M. Blake and I. Fogelman, "Technical principles of dual energy x-ray absorptiometry," *Semin Nucl Med*, vol. 27, pp. 210-28, Jul 1997.
- [31] P. M. Atkinson and C. D. Lloyd, "Non-stationary variogram models for geostatistical sampling optimisation: an empirical investigation using elevation data," *Comput Geosci*, vol. 33, pp. 1285–300, 2007.
- [32] A. B. Mcbratney and R. Webster, "Choosing functions for semi-variograms of soil properties and fitting them to sampling estimates," *J Soil Sci* vol. 37, pp. 617–39, 1986.
- [33] C. C. Stephen, *Bone Mechanics HandBook*, Second ed. New York: Informa Healthcare USA, Inc., 2001.
- [34] G. M. Blake, *et al.*, "Dual energy x-ray absorptiometry: the effects of beam hardening on bone density measurements," *Med Phys*, vol. 19, pp. 459-65, Mar-Apr 1992.
- [35] J. A. Stein, "U.S. Patent and Trademark Office," 1989.
- [36] M. Doube, *et al.*, "BoneJ: Free and extensible bone image analysis in ImageJ," *Bone*, vol. 47, pp. 1076-9, Dec 2010.
- [37] Kazuhisa Takemura, "A Simple Linear Regression Analysis for Fuzzy Input-Output Data and Its Application to Psychological Study " *IEEE International Conference on Intelligent Processing Systems*, pp. 49-53, October 28-31 1997.
- [38] S. L. Bonnick and L. A. Lewis, *Bone densitometry for technologists*. Newyork; London, Springer 2013.
- [39] N. F. Peel, *et al.*, "Impact of anomalous vertebral segmentation on measurements of bone mineral density," *J Bone Miner Res*, vol. 8, pp. 719-23, Jun 1993.
- [40] O. Louis, *et al.*, "Dual-energy X-ray absorptiometry of lumbar vertebrae: relative contribution of body and posterior elements and accuracy in relation with neutron activation analysis," *Bone*, vol. 13, pp. 317-20, 1992.

- [41] X. G. Cheng, *et al.*, "Prediction of vertebral and femoral strength in vitro by bone mineral density measured at different skeletal sites," *J Bone Miner Res*, vol. 13, pp. 1439-43, Sep 1998.
- [42] D. G. Kim, *et al.*, "The effect of regional variations of the trabecular bone properties on the compressive strength of human vertebral bodies," *Ann Biomed Eng*, vol. 35, pp. 1907-13, Nov 2007.
- [43] E. Perilli, *et al.*, "Failure strength of human vertebrae: prediction using bone mineral density measured by DXA and bone volume by micro-CT," *Bone*, vol. 50, pp. 1416-25, Jun 2012.
- [44] J. P. Roux, *et al.*, "Contribution of trabecular and cortical components to biomechanical behavior of human vertebrae: an ex vivo study," *J Bone Miner Res*, vol. 25, pp. 356-61, Feb 2010.
- [45] D. Burr, "Microdamage and bone strength," *Osteoporos Int*, vol. 14 Suppl 5, pp. S67-72, Sep 2003.
- [46] A. M. Parfitt, *et al.*, "Bone histomorphometry: standardization of nomenclature, symbols, and units. Report of the ASBMR Histomorphometry Nomenclature Committee," *J Bone Miner Res*, vol. 2, pp. 595-610, Dec 1987.
- [47] A. Odgaard, "Quantification of cancellous bone architecture," in *Bone mechanics handbook*, S. C. Cowin, Ed., 2nd ed New York: Informa Healthcare, 2009.
- [48] D. Stoyan, *et al.*, *Stochastic geometry and its applications*, 2nd ed. Chichester ; New York: Wiley, 1995.
- [49] X. N. Dong, *et al.*, "Random field assessment of nanoscopic inhomogeneity of bone," *Bone*, vol. 47, pp. 1080-4, Dec 2010.
- [50] D. D. Cody, *et al.*, "Correlations between vertebral regional bone mineral density (rBMD) and whole bone fracture load," *Spine (Phila Pa 1976)*, vol. 16, pp. 146-54, Feb 1991.
- [51] H. F. Boehm, *et al.*, "Prediction of the fracture load of whole proximal femur specimens by topological analysis of the mineral distribution in DXA-scan images," *Bone*, vol. 43, pp. 826-31, Nov 2008.

- [52] T. Beck, "Measuring the structural strength of bones with dual-energy X-ray absorptiometry: principles, technical limitations, and future possibilities," *Osteoporos Int*, vol. 14 Suppl 5, pp. S81-8, Sep 2003.
- [53] T. J. Beck, "Extending DXA beyond bone mineral density: understanding hip structure analysis," *Curr Osteoporos Rep*, vol. 5, pp. 49-55, Jun 2007.
- [54] V. Bousson, *et al.*, "Trabecular bone score (TBS): available knowledge, clinical relevance, and future prospects," *Osteoporos Int*, vol. 23, pp. 1489-501, May 2012.
- [55] B. C. Silva, *et al.*, "Trabecular bone score: a noninvasive analytical method based upon the DXA image," *J Bone Miner Res*, vol. 29, pp. 518-30, Mar 2014.
- [56] J. A. Kanis, *et al.*, "FRAX and the assessment of fracture probability in men and women from the UK," *Osteoporos Int*, vol. 19, pp. 385-97, Apr 2008.
- [57] H. Z. Jerrold, *Biostatistical Analysis*, Fourth ed. NJ: Prentice-Hall, Inc., 1999.

APPENDIX A

CALCULATION OF P-VALUES FOR CORRELATION ANALYSIS

The estimated probability of rejecting the *null hypothesis* (H_0) is called *p-value* [57]. A major goal of statistical analysis is to draw inferences about particular data by examining a sample from that data set. A very common example of this is the desire to draw conclusions about one or more means of that data set. For example, a null hypothesis about a mean (μ) of particular data set might assert that μ is equal to zero. If it is concluded that it is likely that null hypothesis is false, then an *alternate hypothesis* (H_A) is assumed to be true (rejecting the null hypothesis means accepting the alternate hypothesis) [57]. Example conditions for null hypothesis and alternate hypothesis in one tailed and two tailed statistical analyses can be given as,

$$H_0: \mu = 0, H_A: \mu > 0 \quad (\text{One tailed}) \quad A.1$$

$$H_0: \mu = 0, H_A: \mu \neq 0 \quad (\text{Two tailed}) \quad A.2$$

The probability of 5% or less is commonly used as the criterion for rejection of null hypothesis and the probability used as the criterion for rejection is called the *significance level* (α). This means the corresponding correlation is statistically significant when the *p-value* is less than the significance level (5%). The value of the test statistic corresponding to α is termed the *critical value* of the test statistic.

The *p-value* can be estimated using student's *t* distributions in correlation coefficient analyses. In the correlation coefficient analysis the null hypothesis is rejected when the calculated *t* value is greater than or equal to the critical *t* value (which is from the table Critical Values of the *t* Distributions) [57]. 't' value can be calculated as,

$$t = \frac{r}{s_r} \quad A.3$$

where *r* is the correlation coefficient and s_r is the standard error of correlation coefficient.

Appendix A (continued)

The standard error of correlation coefficient may be computed as

$$s_r = \sqrt{\frac{1-r^2}{n-2}} \quad \text{A.4}$$

where r^2 is the correlation index and n is the sample size.

In the correlation coefficient analysis, the null hypothesis is rejected [57] if

$$|t| \geq t_{\alpha(2),v} \quad \text{A.5}$$

where α is the significance level (0.05 or less), v is the degrees of freedom ($n-2$) and 2 specifies two tailed statistical analysis.

For example, the correlation coefficient (r) is equal to 0.870 and n is equal to 12 for particular data set. Then p -value is calculated as follows

$$s_r = \sqrt{\frac{1-(0.870)^2}{12-2}} = 0.156;$$

$$t = \frac{0.870}{0.156} = 5.58; \text{ (calculated value)}$$

$$t_{0.05(2),10} = 2.228 \text{ (critical value from the table)}$$

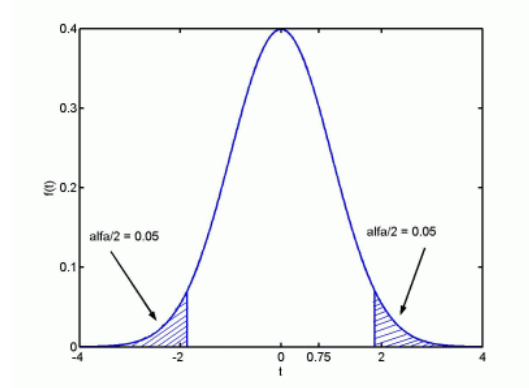


Fig. A.1 Student's t distribution curve

Here the calculated t value is greater than the critical t value. Hence, the null hypothesis is rejected and the p -value should be less than 0.05. The p -value can be estimated from the Critical Values of the t Distributions [57] or it can be computed as

$$p = \int_0^{\infty} \frac{\Gamma(\frac{v+1}{2})}{\sqrt{v\pi} \Gamma(\frac{v}{2})} \left(1 + \frac{x^2}{v}\right)^{-\frac{v+1}{2}} dx \quad \text{A.6}$$

where v is the degrees of freedom, x is the calculated t value, Γ is the gamma function.

APPENDIX B

MATLAB CODE

```

%%%%%%%%%%%%%%%%%%%%%%%%%%%%%%%%%%%%%%%%%%%%%%%%%%%%%%%%%%%%%%%%%%%%%%%% Calculation of experimental variogram %%%%%%%%%%%%%%%%%%%%%%%%%%%%%%%%%%%%%%%%%%%%%%%%%%%%%%%%%%%%%%%%%%%%%%%%%
function S = variogram(x,y,varargin)

% error checking
if size(y,1) ~= size(x,1);
    error('x and y must have the same number of rows')
end
% check if consolidator and ipdm are available
if exist('ipdm.m','file') ~= 2;
    error('IPMD is not available. See help variogram for more infos')
end

% check for nans
II = any(isnan(x),2) | isnan(y);
x(II,:) = [];
y(II) = [];

% extent of dataset
minx = min(x,[],1);
maxx = max(x,[],1);
maxd = sqrt(sum((maxx-minx).^2));
nrdims = size(x,2);

% check input using PARSEARGS
params.nrbins = 20;
params.maxdist = maxd/2;
params.type = {'default','gamma','cloud1','cloud2'};
params.plotit = false;
params.anisotropy = false;
params.thetastep = 30;
params = parseargs(params,varargin{:});

if params.maxdist > maxd;
    warning('Matlab:Variogram',...
        ['Maximum distance exceeds maximum distance \n' ...
        'in the dataset. maxdist was decreased to ' num2str(maxd)
    ]);
    params.maxdist = maxd;
end
if params.anisotropy && nrdims ~= 2
    params.anisotropy = false;
    warning('Matlab:Variogram',...
        'Anistropy is only supported for 2D data');
end
% calculate bin tolerance
tol = params.maxdist/params.nrbins;

% calculate euclidean interpoint distances using ipdm
d = ipdm(x,'Result','Structure',...
    'Subset','Maximum',...

```

Appendix B (continued)

```
'Limit',params.maxdist);

% remove distances where d.columnindex = d.rowindex
iid = [d.rowindex d.columnindex d.distance];

% clear workspace variable
clear d

% remove double entries in iid
iid(iid(:,1) == iid(:,2),:) = [];
[m,m] = unique(sort(iid(:, [1 2]),2), 'rows');
iid = iid(m,:);

% calculate squared difference between values of coordinate pairs
lam      = (y(iid(:,1))-y(iid(:,2))).^2;

% anisotropy
if params.anisotropy
    nrthetaedges = floor(180/params.thetastep);

    % calculate with radians, not degrees
    params.thetastep = params.thetastep/180*pi;

    % calculate angles, note that angle is calculated clockwise from
top
    theta      = atan2(x(iid(:,2),1)-x(iid(:,1),1),...
                      x(iid(:,2),2)-x(iid(:,1),2));

    % only the semicircle is necessary for the directions
    I          = theta < 0;
    theta(I)   = theta(I)+pi;
    I          = theta >= pi-params.thetastep/2;
    theta(I)   = 0;

    % create a vector with edges for binning of theta
    % directions go from 0 to 180 degrees;
    thetaedges = linspace(-params.thetastep/2,pi-
params.thetastep/2,nrthetaedges);

    % bin theta
    [ntheta,ixtheta] = histc(theta,thetaedges);

    % bin centers
    thetacents = thetaedges(1:end)+params.thetastep/2;
    thetacents(end) = pi; %[];
end
% calculate variogram
switch params.type
case {'default','gamma'}
    % variogram anonymous function
    fvar      = @(x) 1./(2*numel(x)) * sum(x);
    % distance bins
    edges      = linspace(0,params.maxdist,params.nrbins+1);
```

Appendix B (continued)

```

edges(end) = inf;

[nedge,ixedge] = histc(iid(:,3),edges);

if params.anisotropy
    S.val = accumarray([ixedge ixtheta],lam,...
        [numel(edges)
numel(thetaedges)],fvar,nan);
    S.val(:,end)=S.val(:,1);
    S.theta = thetacent;
    S.num = accumarray([ixedge
ixtheta],ones(size(lam)),...
        [numel(edges)
numel(thetaedges)],@sum,nan);
    S.num(:,end)=S.num(:,1);
else
    S.val = accumarray(ixedge,lam,[numel(edges)
1],fvar,nan);
    S.num =
accumarray(ixedge,ones(size(lam)),[numel(edges) 1],@sum,nan);
end
S.distance = (edges(1:end-1)+tol/2)';
S.val(end,:) = [];
S.num(end,:) = [];

case 'cloud1'
    edges = linspace(0,params.maxdist,params.nrbins+1);
    edges(end) = inf;

    [nedge,ixedge] = histc(iid(:,3),edges);

    S.distance = edges(ixedge);
    S.val = lam;
    if params.anisotropy
        S.theta = thetacent(ixtheta);
    end
case 'cloud2'
    S.distance = iid(:,3);
    S.val = lam;
    if params.anisotropy
        S.theta = thetacent(ixtheta);
    end
end

% create plot if desired
if params.plotit
    switch params.type
    case {'default','gamma'}
        marker = 'o--';
    otherwise
        marker = '.';
    end
end

```

Appendix B (continued)

```

if ~params.anisotropy
    plot(S.distance, S.val, marker);
    axis([0 params.maxdist 0 max(S.val)*1.1]);
    xlabel('h');
    ylabel('\gamma (h)');
    title('(Semi-)Variogram');
else
    [Xi, Yi] =
pol2cart(repmat(S.theta, numel(S.distance), 1), repmat(S.distance, 1, numel(
S.theta)));
    surf(Xi, Yi, S.val)
    xlabel('h y-direction')
    ylabel('h x-direction')
    zlabel('\gamma (h)')
    title('directional variogram')
%     set(gca, 'DataAspectRatio', [1 1 1/30])
end
end

end

% subfunction parseargs

function X = parseargs(X, varargin)
remaining = nargin-1; % number of arguments other than X
count = 1;
fields = fieldnames(X);
modified = zeros(size(fields));
% Take input arguments two at a time until we run out.
while remaining >= 2
    fieldname = varargin{count};
    fieldind = find(strcmp(fieldname, fields));
    if ~isempty(fieldind)
        oldvalue = getfield(X, fieldname); %#ok
        newvalue = varargin{count+1};
        if iscell(oldvalue)
            % Cell arrays must contain strings, and the new value must
be
            % a string which appears in the list.
            if ~iscellstr(oldvalue)
                error(sprintf('All allowed values for "%s" must be
strings', fieldname)); %#ok
            end
            if ~ischar(newvalue)
                error(sprintf('New value for "%s" must be a
string', fieldname)); %#ok
            end
            if isempty(find(strcmp(oldvalue, newvalue))) %#ok
                error(sprintf('"%s" is not allowed for field
"%s"', newvalue, fieldname)); %#ok
            end
        elseif ~isempty(oldvalue)
            % The caller isn't allowed to change the data type of a
non-empty property,

```

Appendix B (continued)

```
% and scalars must remain as scalars.
if ~strcmp(class(oldvalue),class(newvalue))
    error(sprintf('Cannot change class of field "%s" from
"%s" to "%s"',...
                fieldname,class(oldvalue),class(newvalue))); %#ok
elseif numel(oldvalue)==1 & numel(newvalue)~=1 %#ok
    error(sprintf('New value for "%s" must be a
scalar',fieldname)); %#ok
end
end
X = setfield(X,fieldname,newvalue); %#ok
modified(fieldind) = 1;
else
    error(['Not a valid field name: ' fieldname]);
end
remaining = remaining - 2;
count = count + 2;
end
% Check that we had a value for every name.
if remaining~=0
    error('Odd number of arguments supplied. Name-value pairs
required');
end

% Now find cell arrays which were not modified by the above process,
and select
% the first string.
notmodified = find(~modified);
for i=1:length(notmodified)
    fieldname = fields{notmodified(i)};
    oldvalue = getfield(X,fieldname); %#ok
    if iscell(oldvalue)
        if ~iscellstr(oldvalue)
            error(sprintf('All allowed values for "%s" must be
strings',fieldname)); %#ok
        elseif isempty(oldvalue)
            error(sprintf('Empty cell array not allowed for field
"%s"',fieldname)); %#ok
        end
        X = setfield(X,fieldname,oldvalue{1}); %#ok
    end
end
end
end
```

Appendix B (continued)

```
##### Theoretical model fitting over experimental variogram #####
function [a,c,n,S] = variogramfit(h,gammaexp,a0,c0,numobs,varargin)

% check input arguments
if nargin == 0
    help variogramfit
    return
elseif nargin>0 && nargin < 2;
    error('Variogramfit:inputargs',...
        'wrong number of input arguments');
end
if ~exist('a0','var') || isempty(a0)
    a0 = max(h)*2/3;
end
if ~exist('c0','var') || isempty(c0)
    c0 = max(gammaexp);
end
if ~exist('numobs','var') || isempty(a0)
    numobs = [];
end

% check input parameters
params.model      = 'spherical';
params.nugget     = [];
params.plotit     = true;
params.solver     = {'fminsearchbnd','fminsearch'};
params.stablealpha = 1.5;
params.weightfun  = {'none','cressie85','mcbratney86'};
params.nu        = 1;
params = parseargs(params,varargin{:});

% check if fminsearchbnd is in the search path
switch lower(params.solver)
case 'fminsearchbnd'
    if ~exist('fminsearchbnd.m','file')==2
        params.solver = 'fminsearch';
        warning('Variogramfit:fminsearchbnd',...
            'fminsearchbnd was not found. fminsearch is used instead')
    end
end

% check if h and gammaexp are vectors and have the same size
if ~isvector(h) || ~isvector(gammaexp)
    error('Variogramfit:inputargs',...
        'h and gammaexp must be vectors');
end

% force column vectors
h = h(:);
gammaexp = gammaexp(:);

% check size of supplied vectors
if numel(h) ~= numel(gammaexp)
```


Appendix B (continued)

```
error('Variogramfit:inputargs',...
      'h and gammaexp must have same size');
end

% remove nans;
nans = isnan(h) | isnan(gammaexp);
if any(nans);
    h(nans) = [];
    gammaexp(nans) = [];
    if ~isempty(numobs)
        numobs(nans) = [];
    end
end

% check weight inputs
if isempty(numobs);
    params.weightfun = 'none';
end

% create options for fminsearch
options = optimset('MaxFunEvals',1000000);
% create vector with initial values
% b(1) range
% b(2) sill
% b(3) nugget if supplied
b0 = [a0 c0 params.nugget];

% variogram function definitions
switch lower(params.model)
case 'spherical'
    type = 'bounded';
    func = @(b,h)b(2)*((3*h./(2*b(1)))-1/2*(h./b(1)).^3);
case 'pentaspherical'
    type = 'bounded';
    func = @(b,h)b(2)*(15*h./(8*b(1))-
5/4*(h./b(1)).^3+3/8*(h./b(1)).^5);
case 'bilinear'
    type = 'bounded';
    func = @(b,h)b(2)*(h./b(1));
case 'circular'
    type = 'bounded';
    func = @(b,h)b(2)*(1-
(2./pi)*acos(h./b(1))+2*h/(pi*b(1)).*sqrt(1-(h.^2)/(b(1)^2)));
case 'exponential'
    type = 'unbounded';
    func = @(b,h)b(2)*(1-exp(-h./b(1)));
case 'gaussian'
    type = 'unbounded';
    func = @(b,h)b(2)*(1-exp(-(h.^2)/(b(1)^2)));
case 'stable'
    type = 'unbounded';
    stablealpha = params.stablealpha;
```

Appendix B (continued)

```
func = @(b,h)b(2)*(1-exp(-(h.^stablealpha)/(b(1)^stablealpha)));
case 'whittle'
    type = 'unbounded';
    func = @(b,h)b(2)*(1-h/b(1).*besselk(1,h/b(1)));
case 'matern'
    type = 'unbounded';
    func = @(b,h)b(2)*(1-(1/((2^(params.nu-1))*gamma(params.nu))) *
(h/b(1)).^params.nu .* besselk(params.nu,h/b(1)));
case 'hole-effect'
    type = 'unbounded';
    func = @(b, h) (b(2)*(1-(sin(h.*pi/b(1))./(h.*pi/b(1)))));
otherwise
    error('unknown model')
end

% check if there are zero distances
% if yes, remove them, since the besselk function returns nan for
% zero
switch lower(params.model)
case {'whittle','matern'}
    izero = h==0;
    if any(izero)
        flagzerodistances = true;
    else
        flagzerodistances = false;
    end
otherwise
    flagzerodistances = false;
end

% if model type is unbounded, then the parameter b(1) is r, which is
% approximately range/3.
switch type
case 'unbounded'
    b0(1) = b0(1)/3;
end

% nugget variance
if isempty(params.nugget)
    nugget = false;
    funnugget = @(b) 0;
else
    nugget = true;
    funnugget = @(b) b(3);
end

% generate upper and lower bounds when fminsearchbnd is used
switch lower(params.solver)
case {'fminsearchbnd'};
    % lower bounds
    lb = zeros(size(b0));
    % upper bounds
```

Appendix B (continued)

```
        if nugget;
            ub = [inf max(gammaexp) max(gammaexp)]; %
        else
            ub = [inf max(gammaexp)];
        end
    end

    % create weights (see Webster and Oliver)
    switch params.weightfun
        case 'cressie85'
            weights = @(b,h)
                (numobs./variofun(b,h).^2)./sum(numobs./variofun(b,h).^2);
        case 'mcbratney86'
            weights = @(b,h)
                (numobs.*gammaexp./variofun(b,h).^3)/sum(numobs.*gammaexp./variofun(b,h).^3);
        otherwise
            weights = @(b,h) 1;
    end

    % create objective function: weighted least square
    objectfun = @(b) sum(((variofun(b,h)-gammaexp).^2).*weights(b,h));

    % call solver
    switch lower(params.solver)
        case 'fminsearch'
            % call fminsearch
            [b,fval,exitflag,output] = fminsearch(objectfun,b0,options);
        case 'fminsearchbnd'
            % call fminsearchbnd
            [b,fval,exitflag,output] =
                fminsearchbnd(objectfun,b0,lb,ub,options);
        otherwise
            error('Variogramfit:Solver','unknown or unsupported solver')
    end

    % prepare output
    a = b(1); %range
    c = b(2); %sill
    if nugget;
        n = b(3); %nugget
    else
        n = [];
    end

    % Create structure array with results
    if nargout == 4;
        S.model = lower(params.model); % model
        S.func = func;
        S.type = type;
        switch S.model
            case 'matern';
                S.nu = params.nu;
            case 'stable';
```

Appendix B (continued)

```
S.stablealpha = params.stablealpha;
end

S.range      = a;
S.sill       = c;
S.nugget     = n;
S.h          = h; % distance
S.gamma      = gammaexp; % experimental values
S.gammahat   = variofun(b,h); % estimated values
S.residuals  = gammaexp-S.gammahat; % residuals
COVyhaty     = cov(S.gammahat,gammaexp);
S.Rs         = (COVyhaty(2).^2) ./...
              (var(S.gammahat).*var(gammaexp)); % Rsquare
S.weights    = weights(b,h); %weights
S.weightfun  = params.weightfun;
S.exitflag   = exitflag; % exitflag (see doc fminsearch)
S.algorithm  = output.algorithm;
S.funcCount  = output.funcCount;
S.iterations = output.iterations;
S.message    = output.message;
end

% if you want to plot the results...
if params.plotit
    switch lower(type)
        case 'bounded'
            plot(h,gammaexp,'rs','MarkerSize',10);
            hold on
            fplot(@(h) funnugget(b) + func(b,h),[0 b(1)])
            fplot(@(h) funnugget(b) + b(2),[b(1) max(h)])

        case 'unbounded'
            plot(h,gammaexp,'rs','MarkerSize',10);
            hold on
            fplot(@(h) funnugget(b) + func(b,h),[0 max(h)])
    end
    axis([0 max(h) 0 max(gammaexp)])
    xlabel('lag distance h')
    ylabel('\gamma(h)')
    hold off
end

% fitting functions for fminsearch/bnd
function gammahat = variofun(b,h)

    switch type
        % bounded model
        case 'bounded'
            I = h<=b(1);
            gammahat = zeros(size(I));
            gammahat(I) = funnugget(b) + func(b,h(I));
            gammahat(~I) = funnugget(b) + b(2);
        % unbounded model
```

Appendix B (continued)

```

        case 'unbounded'
            gammahat = funnugget(b) + func(b,h);
            if flagzerodistances
                gammahat(izero) = funnugget(b);
            end
        end
    end
end
end
% subfunction parseargs
function X = parseargs(X,varargin)

remaining = nargin-1; % number of arguments other than X
count = 1;
fields = fieldnames(X);
modified = zeros(size(fields));
% Take input arguments two at a time until we run out.
while remaining>=2
    fieldname = varargin{count};
    fieldind = find(strcmp(fieldname,fields));
    if ~isempty(fieldind)
        oldvalue = getfield(X,fieldname); %#ok
        newvalue = varargin{count+1};
        if iscell(oldvalue)
            % Cell arrays must contain strings, and the new value must
            be
            % a string which appears in the list.
            if ~iscellstr(oldvalue)
                error(sprintf('All allowed values for "%s" must be
strings',fieldname)); %#ok
            end
            if ~ischar(newvalue)
                error(sprintf('New value for "%s" must be a
string',fieldname)); %#ok
            end
            if isempty(find(strcmp(oldvalue,newvalue))) %#ok
                error(sprintf('"%s" is not allowed for field
"%s"',newvalue,fieldname)); %#ok
            end
            elseif ~isempty(oldvalue)
                % The caller isn't allowed to change the data type of a
non-empty property,
                % and scalars must remain as scalars.
                if ~strcmp(class(oldvalue),class(newvalue))
                    error(sprintf('Cannot change class of field "%s" from
"%s" to "%s"',...
                                fieldname,class(oldvalue),class(newvalue))); %#ok
                elseif numel(oldvalue)==1 & numel(newvalue)~=1 %#ok
                    error(sprintf('New value for "%s" must be a
scalar',fieldname)); %#ok
                end
            end
            X = setfield(X,fieldname,newvalue); %#ok
            modified(fieldind) = 1;
        else

```

Appendix B (continued)

```
        error(['Not a valid field name: ' fieldname]);
    end
    remaining = remaining - 2;
    count = count + 2;
end
% Check that we had a value for every name.
if remaining~=0
    error('Odd number of arguments supplied. Name-value pairs
required');
end

% Now find cell arrays which were not modified by the above process,
and select
% the first string.
notmodified = find(~modified);
for i=1:length(notmodified)
    fieldname = fields{notmodified(i)};
    oldvalue = getfield(X,fieldname); %#ok
    if iscell(oldvalue)
        if ~iscellstr(oldvalue)
            error(sprintf('All allowed values for "%s" must be
strings',fieldname)); %#ok
        elseif isempty(oldvalue)
            error(sprintf('Empty cell array not allowed for field
"%s"',fieldname)); %#ok
        end
        X = setfield(X,fieldname,oldvalue{1}); %#ok
    end
end
end
end
```